FR0201572

EUR-CEA-FC-1723

Towards fully non-inductive current drive operation in JET

X. Litaudon, J.F. Artaud, V. Basiuk, A. Becoulet, M. Becoulet, L.G. Eriksson, C. Fourment, X. Garbet, C. Giroud, G. Huysmans, F. Imbeaux, E. Joffrin, Ph. Lotte, P. Maget, D. Mazon, D. Moreau, F. Rimini, Y. Sarazin, G. Tresset, X. The jet-efda team

January 2002

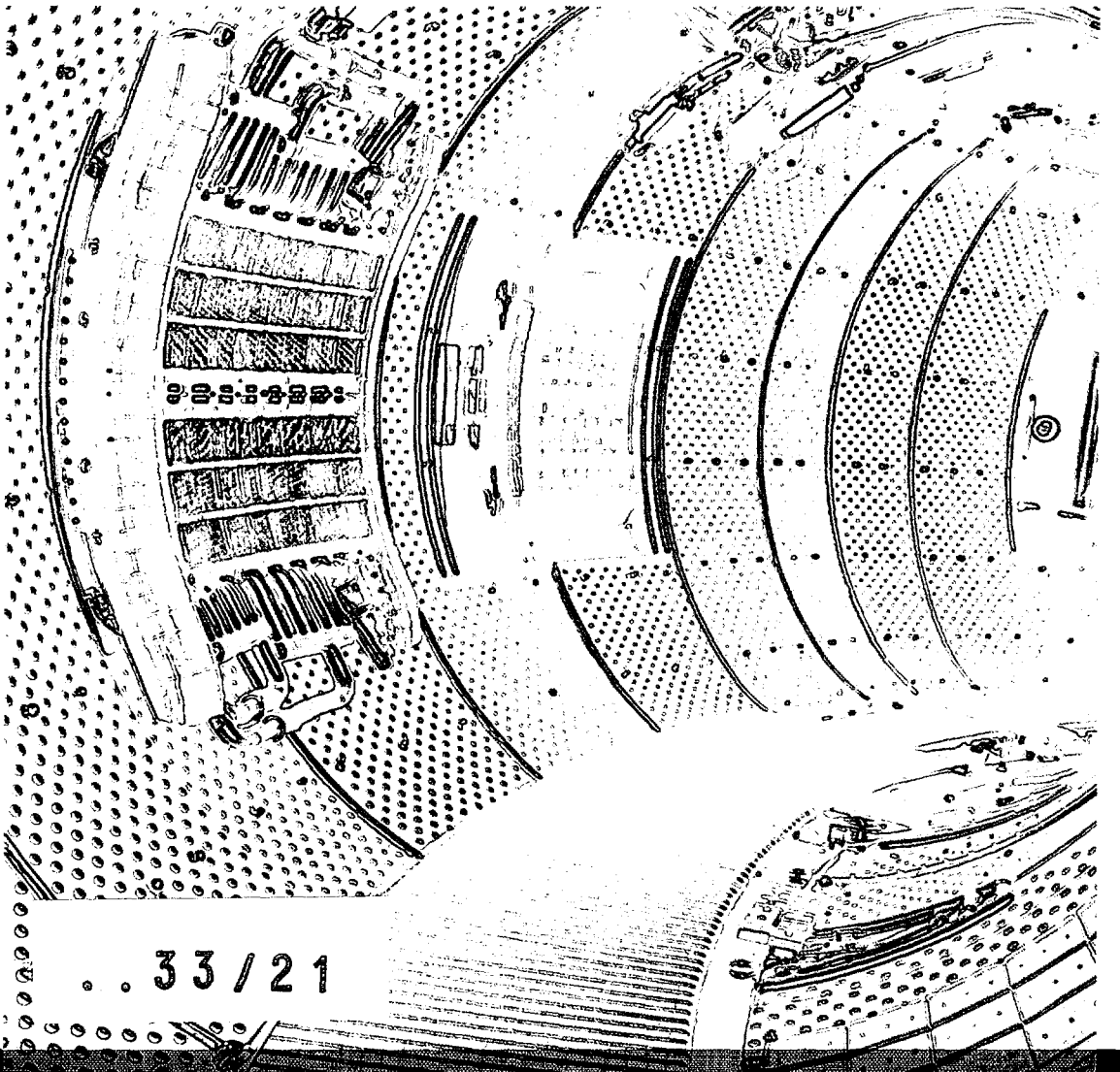

Association EURATOM-CEA sur la Fusion Contrôlée
Département de Recherches sur la Fusion Contrôlée
CEA/Cadarache
F-13108 Saint Paul Lez Durance - FRANCE

Towards fully non-inductive current drive operation in JET*

X. Litaudon[1], F. Crisanti[2], B. Alper[3], J. F. Artaud[1], Yu. F. Baranov[3], E. Barbato[2], V. Basiuk[1], A. Bécoulet[1], M. Bécoulet[1], C. Castaldo[2], C. D. Challis[3], G. D. Conway[4], R. Dux[4], L. G. Eriksson[1], B. Esposito[2], C. Fourment[1], D. Frigione[2], X. Garbet[1], C. Giroud[1], N.C. Hawkes[3], P. Hennequin[1], G. T. A. Huysmans[1], F. Imbeaux[1], E. Joffrin[1], P.J. Lomas[3], Ph. Lotte[1], P. Maget[1], M. Mantsinen[5], J. Mailloux[3], D. Mazon[1], F. Milani[3], D. Moreau[1], V. Parail[3], E. Pohn[6], F. G. Rimini[1], Y. Sarazin[1], G. Tresset[1], K. D. Zastrow[3], M. Zerbini[2] and contributors to the EFDA-JET workprogramme**.

[1]Association EURATOM-CEA, Département de Recherches sur la Fusion contrôlée, CEA Cadarache, F-13108, S[t] Paul lez Durance, France

[2]Associazione EURATOM-ENEA sulla Fusione, Centro Ricerche Frascati, C.P. 65, 00044-Frascati, Italy

[3]Euratom-UKAEA Fusion Association, Culham Science Centre, Abingdon, Oxon, OX14 3DB, UK

[4]IPP-EURATOM Assoziation, Max-Planck-Institut für Plasmaphysik, Boltzmann-Str.2, D-85748 Garching, Germany

[5]Association Euratom-Tekes, Espoo, Finland

[6]Association EURATOM-ÖAW, ÖAW-EURATOM Coordination Office, Kegelgasse 27/3, A-1030 Wien

Submitted to Plasma Physics and Controlled Fusion

* *This paper is an extended version of a contribution to the 28[th] EPS Conference on Controlled Fusion and Plasma Physics, held at Funchal, Madeira, Portugal, June 2001.*

** *See appendix of J. Paméla et al, Fusion Energy 2000 (Proc. 18th Int. Conf. on Fusion Energy, Sorrento 2000), IAEA, Vienna.*

Abstract

Quasi steady operation has been achieved at JET in the high confinement regime with Internal Transport Barriers, ITBs. The ITBs' performances are maintained up to 11s. This duration, much larger than the energy confinement time, is already approaching a current resistive time. The high performance phase is limited only by plant constraints. The radial profiles of the thermal electron and ion pressures have steep gradients typically at mid-plasma radius. A large fraction of non-inductive current (above 80%) is sustained throughout the high performance phase with a poloidal beta exceeding unity. The safety factor profile plays an important role in sustaining the ITB characteristics. In this regime where the self-generated bootstrap current (up to 1.0MA) represents 50% of the total current, the resistive evolution of the non-monotonic q-profile is slowed down by using off-axis lower hybrid current drive.

1. Introduction

Improvement of the tokamak concept in terms of confinement and stability is a crucial challenge which could lead to operating the device in a continuous mode (Kikuchi 1990). In present day experiments and in the design of next step tokamaks, the gain in confinement and fusion power is through the favourable scaling of the energy confinement time with the plasma current. In this context, steady state operation would require large non-inductive current drive. In such conditions it has been recognised that an efficient steady state thermonuclear reactor where the amount of recirculating power for external current drive is minimised would need current drive efficiency which is practically an order of magnitude larger than presently achieved (Rebut et al 1993). The development of steady state operational regime at reduced plasma current with the potential of a simultaneous increase in the confinement enhancement factor and plasma pressure is known as "advanced tokamak" research (this research is reviewed in e. g. Burrel 1997, Taylor 1997, Litaudon 1998, Synakowski 1998, Gormezano 1999, Kamada 2000). Higher confinement plasmas properties with respect to standard scaling laws appear promising for reducing the plasma current and increasing the self-generated bootstrap current. In a steady state tokamak reactor where the plasma current is entirely sustained by non-inductive means, the bootstrap current would provide a significant fraction of the plasma current to reduce the external current drive requirement. Significant enhancement of the tokamak performance could be obtained by combining a narrow transport barrier at the plasma edge (H-mode) with a reduction of the anomalous transport over the core region known as Internal Transport Barrier (ITB). Following this approach, high performance in terms of confinement and fusion yield has been obtained in ASDEX-U (Wolf et al 1999), DIII-D (Strait et al 1995), FT-U (Alladio et al 2000), JET (JET Team 1999), JT-60 (Ishida et al 1997), Tore Supra (Hoang et al 2000), TFTR (Levinton et al 1995). In most of these experiments the improvement of the tokamak performance is generally the result of a

rapid change of the plasma parameters and are transient in nature. For instance, the optimised current density profiles for reducing the anomalous transport over the plasma core are the result of a rapid rise of the plasma current. A major challenge still remains to extend these improvements in confinement towards steady state regime. Initial experiments where the modified current profiles are maintained in stationary conditions with external current drive such as Lower Hybrid wave were carried out but at modest value of normalised toroidal beta (e.g. Equipe Tore Supra 1996, Ide et al 1996). Experimental effort focus nowadays in maintaining stationary conditions at high pressure with the corresponding high bootstrap current (Kikuchi et al 2001). The main issue is to find and ultimately control the optimum combination of pressure and current density profiles compatible with high energy confinement time, high normalised toroidal beta, β_N, and a large fraction of bootstrap current. Within the framework of this activity, we report in this paper on the recent progress achieved on JET in view of maintaining the ITB regime with a high fraction of non-inductive current on a time scale comparable to a resistive time (Crisanti et al 2001).

The paper is organised as follows. We describe in section 2 the operating conditions and experimental scenario. To investigate the physics of full current drive operation, regime with Internal Transport Barriers has been investigated at reduced plasma current. Two series of experiments are reported in this section where the self generated bootstrap current is combined with only the neutral beam current drive (NBCD) (first set of experiments) or with the sum of NBCD and off-axis Lower Hybrid Current Drive, LHCD (second set of experiments). In section 3, a statistical analysis of the database consisting of the highly non-inductive discharges is used to describe the global trend and performances. Then in section 4, we report on a comprehensive analysis of the current resistive evolution in order to assess the various non-inductive currents. Finally in section 5, the thermal ion and electron local transport coefficients are evaluated together with the evolution of the radial electric field and its shear inside the plasma. The linear growth rates of the plasma microinstabilities are evaluated and the direct role of the q-profile in the stabilisation process of the long wavelength modes is also discussed in this last section.

2. Description of the experimental scenario

2.1. Operating conditions and plasma diagnostics

We report in this paper experiments carried out on JET during the 2000-2001 campaign where the improved confinement regime with Internal Transport Barrier is maintained with a large fraction of non-inductive current. The experimental conditions are as follows : Mark II Gas-Box divertor with single-null X point magnetic configuration, Deuterium plasmas, an elongation of 1.7, averaged triangularity δ=0.2, toroidal magnetic field, B_o=3.45T, at the geometrical center of the plasma boundary R_o=2.9m, a minor radius of a=0.95m, reduced plasma current plateau ranging from I_p=1.5MA to 2MA corresponding to a

safety factor between q_{95}=8 and q_{95}=5.5 at 95% of the poloidal flux. The plasma discharges are heated with a combination of Neutral Beam Injection (NBI), Ion Cyclotron Resonance Heating (ICRH) using hydrogen minority heating scheme with the resonance located near the plasma centre (f=51MHz), and Lower Hybrid power (f=3.7GHz). The plasma pressure normalised to the magnetic field pressure is extensively used in this paper to characterise the discharge performances. The poloidal and toroidal beta parameters are respectively defined as $\beta_p = 2\mu_o \langle p \rangle / B_p^2$ and $\beta_t = 2\mu_o \langle p \rangle / B_o^2$ where $\langle p \rangle$ is the volume averaged total plasma pressure and B_p is the averaged poloidal magnetic field on the plasma surface. The normalised toroidal beta is defined as $\beta_N = (I_p/aB_o)^{-1} \beta_t$.

The operational scenario consists in two distinguishing phases: a low power prelude phase, devoted to shape the current density profile, followed by a high performance phase where the full heating and current drive powers are applied (Sips et al 1998, JET Team 1999). The precise optimisation and time sequence of the application of the various powers will be described in the parts 2-2 and 2-3. In this paragraph, we focus our attention on the new operational aspects directly linked to the control at high poloidal beta of the plasma position. Indeed, it was found in previous experiments that high performance phases could suddenly be interrupted without any MHD activity when the plasma boundary was interacting with the septum parts of the Gas-Box divertor (Gormezano et al 2000). The X-point configuration is formed in the low beta phase typically one second after the plasma initiation while the current is ramped. When increasing the Shafranov shift at high poloidal beta a key difficulty is to develop a configuration avoiding plasma interaction with the septum. In experiments reported in this paper, the positions of the X-point and strike points are feedback controlled at prescribed values with the outermost divertor coils currents that compensate in real time the plasma displacement arising from an increase of the core pressure and Shafranov shift. The purpose of this feedback scheme is to minimise interaction between the septum plates of the divertor and the plasmas fluxes when high poloidal beta, β_p, values are sustained while keeping an optimum pumping conditions by the divertor cryo-pumps. Thanks to this control a similar magnetic configuration close to the divertor septum is obtained for two ITB discharges but with low and high poloidal beta reaching up to β_p=1.65, as shown on figure 1. This figure indicates that the strike points are maintained in the entrance to the divertor pump ducts to maximise the pumping efficiency and maintain a low edge density ("corner configuration") while interaction of the X-point with the septum parts of the divertor is avoided.

In this paragraph, we briefly recall the main diagnostics used to characterise and analyse the results described in this paper. The electron temperature profile, T_e, is measured simultaneously by the Thomson scattering system and the electron cyclotron emission (ECE) heterodyne radiometer. The ECE diagnostic is well suited to characterise the physics of the internal transport barrier due to its high resolution : routinely 2cm with a time resolution of 0.5ms. The LIDAR Thomson scattering diagnostic is mainly used for the measurement of the electron density profile, n_e, taken every 250ms with a radial resolution of

±6cm. The ion temperature profile, T_i, the toroidal rotation, V_ϕ, and the carbon density profiles are measured with the charge exchange spectroscopy (CXS) diagnostic that has a radial and time resolution of respectively 10cm and 50ms. The plasma equilibrium and the associated quantities such as the magnetic safety factor profile, q, are identified by solving the Grad-Shafranov equation with the EFIT code (Lao et al 1990) constrained by the magnetic data from pick-up coils and flux-loops located at the vacuum vessels of the torus. In addition, for an accurate determination of the q-profile in the plasma core, the solution of the Grad-Shafranov equation is also subject to constraint from the Faraday rotation data (8 line of sights of the far-infrared polarimetry diagnostic) or the motional Stark effect measurements (25 spatial channels) of the recently installed diagnostic (Hawkes et al 1999, Hawkes et al 2001a-b). Emphasis is given on the accurate determination of the q-profile and its shear, s, [$s = \rho/q\ (dq/d\rho)$ with ρ the flux coordinate] since these profiles play a critical role in the characteristics and sustainment of the plasmas with Internal Transport Barrier (c.f. section 5). In the analyses presented in this paper, the measurement of the Faraday rotation angles are mainly used to assess the q-profile evolution during the high power NBI heating phase when all the injector sources were operated. Indeed, in this phase the parasitic intensities from all beam lights intersecting the line of sight of the MSE (Motional Stark Effect) diagnostic prevent from an accurate measurement of the magnetic pitch angles. On the other hand, the q-profile is accurately deduced from the MSE data during the prelude phase at reduced NBI power where the injector sources are carefully selected for the MSE diagnostic purpose.

2.2. Sustainment of ITB with bootstrap and neutral beam current drive

An important and open issue is the optimisation of the route towards a genuine steady state regime where the required current profile for improved confinement and stability is the sum of the different non-inductive currents. The chosen strategy consists in forming a non-monotonic q-profile in the low β_p phase of the discharge by coupling 2-3MW of LH power soon after the plasma initiation (Challis et al 2001a, Hawkes et al 2001, Huysmans et al 2001) while the current is ramped at a rate of 0.4MA/s up to its flat top value, 1.5MA at B_o=3.45T (figure 2). The reduced value of plasma current has been chosen to increase the poloidal beta and the bootstrap current fraction (Kessel 1994). The value of the toroidal field has been fixed based on simple zero-dimensional analysis. Optimising the bootstrap current fraction requires to obtain simultaneously high β_N at high safety factor ($\sim B_o/I_p$), i.e. high β_N at high toroidal field and at reduced plasma current. Indeed, the bootstrap current fraction is proportional to the poloidal beta that is expressed as the product of β_N times the edge safety factor. In addition, the toroidal field has been chosen to a relatively high value for JET to increase the L to H mode power threshold. Indeed, for the same current ramp-up rate the high q_{95} regime requires to apply the full heating power in the current plateau in contrast to previous JET optimised shear operation mainly performed at q_{95}=3 (JET Team 1999).

Therefore as pointed in (Gormezano et al 2000), the problem when reaching high β_p is not only to develop a configuration avoiding septum interaction (c.f. section 2.1), but also to prevent the appearance of strong ELMs (Edge Localised Modes) which are generally triggered without a current ramp-up at power level much larger than the L to H mode power threshold (Sarazin et al 2001b).

In conditions with reduced current operation, the tuning of the target q-profile relies on both the current ramp and on the LHCD power in particular when the current plateau is reached so as to delay the inward diffusion of the plasma current. The target q-profile is measured at the time of application of the NBI and ICRH powers, i.e. at the start of the high power phase. The power waveforms and electron density during the pre-heat phase have been varied to tune this target q-profile. The NBI/ICRH power waveform has been chosen from a set of dedicated experiments where the application time has been varied while keeping all the other parameters fixed. The chosen time corresponds to the case where plasma performance in terms of neutron rate, core pressure and confinement is maximum. In the discharge shown on figure 2, the full heating power (up to 20MW) consisting of Ion Cyclotron Resonance Heating (ICRH, 5MW) and NB Injection is applied at t=4.1s during 5.5s to form an internal transport barrier while the LH power is switched-off. In particular, one of the purpose of the optimisation of the target q-profile is to avoid the development of (double) tearing MHD modes (n=1) during the high power phase (Hennequin et al 2001). Once triggered, these mode may persist during the whole heating phase and consequently inhibit the formation of the ITBs. This is the case for the pulse #51780 (figure 3) where a long lived tearing mode activity is recorded throughout the main heating phase. The mode structure was confirmed using the fast magnetic together with the ECE data and the inferred location of the m/n=3/1 island is indicated on the target q-profile shown on figure 4. Indeed, it is worth noting that the spectrogram of the magnetic probe signals shows a multi-harmonic signature. For this pulse the only operational difference compared to the successful discharges (dashed line on figure 3) is the slightly different density in the pre-heating phase. Indeed, the target density is affecting the q-profile evolution in the pre-heat phase by varying both the electron temperature and the LH driven current value.

In the successful discharges as shown on figure 2, the loop voltage at the plasma surface, V_s, drops down to zero during the high power phase thanks to the build-up of the plasma pressure and the rise of the poloidal beta up to 1.65. The target q-profile at the time of the application of the full power is weakly reversed with a minimum q-value, q_{min}, close to three at mid-plasma radius as inferred from the equilibrium reconstruction code EFIT constrained by the MSE data (figure 4). The zero loop voltage is maintained during one second from t=7.4s to 8.4s in the 1.5MA current plateau with a core density of $3.310^{19}m^{-3}$, an improved energy confinement time factor of respectively $H_{ITER\text{-}89P}$=2.5 according to ITER-89P non-thermal L-mode scaling law (as revised by Kaye et al 1994) and $H_{ITER97\text{-}H}$=1 for the thermal H-mode scaling (ITER97-H) at a normalised toroidal beta, $\beta_N \approx 2$. The phase with V_s=0V is terminated by a roll-over of the core performance (inside 0.4 in normalised radius) when q_{min} approaches two and reduces

the amount of bootstrap current (β_p drops down to 1.4). Nevertheless, the flux consumption at the plasma boundary is less than 0.02Wb during the high power phase. The improved confinement is due to a combination of an edge and a core transport barrier located at two third of the plasma radius. Although the total applied power is at least a factor two above the power threshold to trigger large amplitudes type I ELMs, the mild ELM activity keeps a type-III behaviour in the current plateau phase without injecting radiative gases for edge cooling. The electron pedestal pressure stays below 6kPa and the ELM activity does not affect the ITB performance. This is one of the striking and unexpected results of these experiments. A possible explanation for the type I ELM avoidance is the larger edge current fraction in the ITB discharges with broad current density profiles compared to standard H-mode operation (Bécoulet M. et al 2001, Sarazin et al 2001b). The larger edge current fraction is self-sustained throughout the high power phase without ohmic current ramps since a larger fraction of off-axis non-inductive current is driven in these discharges.

During the five seconds of the high power phase the internal inductance, l_i, remains low indicating that a broad current density profile is maintained in this non-inductive phase. Nevertheless, the q-profile identified with EFIT from the time evolution of the Faraday rotation angles evolves slowly towards a monotonic profile with q-on axis, q_o, approaching two (figure 5). The slow redistribution of the current density profile is invoked to explain the core performance roll-over at $t\approx5.2$s and $t\approx7.8$s (c.f. the time trace of the neutron rate) since at these times q_o is approaching respectively three and two. MHD analyses indicate the presence of a medium n ($n\geq2$) tearing mode activity as previously observed in ITB discharges with monotonic q-profiles and weak central magnetic shear (Baranov et al 1999, Hender et al 1999). Figure 5 shows also that the ITB is located in the positive shear region around the rational q=3 surface (Challis et al 2001a). Consistently, the density fluctuation measurement from the reflectometry diagnostic indicates a drop of fluctuation at this location. The ITB characteristics are shown for instance on the toroidal rotation profiles but similar features are also observed on the ion and electron temperature radial profiles.

2.3. Sustainment of ITB with lower hybrid current drive in high power discharges

A similar approach towards stationary operation has been investigated but by maintaining the LH power during the high power ELMy H-mode phase in order to further slow down the current profile evolution and avoid q_{min} crossing two. Successful coupling of the LH waves up to 3MW during the H-mode phase with reflected power in the range of 5% has been obtained by controlling the local density at the grill aperture by injecting CD_4 gas from a valve magnetically connected to the LH antenna (Tuccillo et al 2001, Ekedahl et al 2001).

One of the longest pulse with LH power combining an ELMy H-mode edge (type III) and core transport barrier sustained with a loop voltage approaching zero at a plasma current plateau of 2MA is shown on figure 6 (#53521, q_{95}=5.5, $H_{ITER\text{-}89P}$=2, $H_{ITER97\text{-}H}$=0.95, β_p=1.1, β_N=1.7 at B_o=3.45T). The CD_4 gas is injected at a constant level of $7.5x10^{21}$electrons/s between t=4s and t=12.5s with the launcher positionned 1cm behind the poloidal limiter at an averaged distance from the plasma separatrix of 5.5cm. As in the previous experiments described in section 2.2, the ELMs keep a mild activity with a type III behaviour even during the current plateau. In this discharge, the electron ITB is maintained during 11s from the LH preheat phase up to the pre-programmed end of the power waveforms. This is the longest discharge during which an ITB has been sustained on JET and this duration corresponds approximately to 37 energy confinement time, τ_E. The ITB observed on the ion temperature, electron density and toroidal rotation profile is sustained during the whole high power phase (≈8s, ≈27τ_E). This phase starts at t=4.2s and consists of a combination of 15MW of NBI, 4MW of ICRH and 2.7MW of LHCD powers. In this phase, all the heating and current drive systems presently available at JET have been used simultaneously and the injected energy is 193MJ. Those ITB durations become comparable to the volume averaged resistive current diffusion time, $\tau_R=\langle\mu_o\sigma(\rho)\rho^2\rangle$, evaluated with the local neo-classical conductivity profile, $\sigma(\rho)$. During the LH preheat phase, the ITB on the electron temperature profile is located at a normalised radius of ρ/ρ_{max}=0.2-3 (Hogeweij et al 2001, Mailloux et al 2001, Conway et al 2001) and then expands radially up to 0.45 in the high beta phase. Similar location of the ITB is observed on the electron density profile rising up to $n_{eo}=6.010^{19}m^{-3}$, ion temperature, and toroidal rotation (see figure 7). Finally, it should be pointed out that the duration of this discharge is close to the JET technical operational limits fixed by the maximum duration of application of the full NBI power and the high toroidal field operation at B_o=3.45T.

The target q-profile at t=4.2-4.3s is reversed with q_{min}≈3 at ρ/ρ_{max}≈0.5 as inferred from MSE measurements (figure 8, open triangles). In these specific operating conditions, the target q-profile has also been tuned either by changing (i) the time of application of the NBI and ICRH powers or (ii) the level of LHCD power prior to the high power phase. This study is briefly summarised on Figure 8. The target q-profile measured 0.5s earlier compared to the reference pulse #53521 (figure 8, open circles) is deeply reversed ($q_o \geq q_{95}$) with the minimum q surface at mid-radius. For the same conditions, a reduction of the LH power down to 1MW strongly modifies the target q-profile, i.e. the minimum q-surface is closer to the magnetic axis and the q-profile is weakly reversed. Delaying the application of the high heating powers to t=5s (figure 8, open squares) has the effect of shifting the whole target q-profile down to lower values compared to the reference pulse (open triangles): in particular, q_{min} located at approximately the same radius is decreased from 3 down to 2.5.

The q-profile evolution is assessed with the help of the EFIT code constrained by the FIR polarimetry data taken at various selected times during the discharges (figure 9). We have first checked

that the target q-profiles inferred with EFIT constrained either by the MSE or the FIR polarimetry data are in agreement (figure 9, top). Then, in the high power phase the FIR polarimetry data indicates that q_o slowly decreases from 4 down to 2.7 consistently with the slow evolution of l_i. Nevertheless, the q-profiles keep a non-monotonic shape with q_{min} maintained above 2 at mid-radius thanks to the high fraction of non-inductive current reaching up to 90% of the total current as it will be calculated in section 4. The freezing of the q-profile evolution, in particular the location and value of q_{min}, allows to maintain the ITBs inside mid-plasma radius, i.e. in the weak or negative magnetic shear region.

A more detailed analysis of the time evolution of the various profiles indicates that temperature collapses from which the ITB spontaneously recovers could occur both in the low and high beta phase of the discharge. The dynamics of the electron ITB is well depicted by representing on figure 10 the space-time domain where the normalised electron temperature gradient exceeds a threshold value (Tresset et al 2001). Indeed it was found that an ITB exists at radius R and time t when $\rho_T^*(R,t)=\rho_s/L_T \geq \rho_{ITB}^*$, i.e. the local temperature gradient scale length, $L_T=-[\partial T/\partial R]/T$, normalised to the ion Larmor radius at the sound speed, ρ_s, exceeds the critical value, ρ_{ITB}^*. This critical constant has been determined from a previous detailed analysis of the JET database and fixed at 1.410^{-2}. The estimate of the ITB criterion includes the errors on the measurements and the figure of merit of the ITB is referred to as a confidence factor for identifying an ITB, i.e. a probability that ρ_T^* exceeds the critical value (a confidence level of 50% is obtained when the expectation value of $\rho_T^*(R,t)$ equals ρ_{ITB}^*). Figure 10 shows the constant contours of the confidence levels in the $(t, \rho/\rho_{max})$ plane. The constant contour are only plotted when the confidence level is above 50%. In the same plane, the location of the q_{min} surface is also plotted confirming that the ITB is maintained inside this radius. In the LHCD phase alone ($t<4.2s$), electron temperature collapses (high q sawtoothing behaviour) are associated to a double tearing mode activity. During the high power phase, two major core collapses occur at t=6.7s and t=11.1s from which the ITB recovers immediately after. The first one (large n=1 MHD burst) is attributed to a n=1 ideal mode with a global structure located between the two q=3 rational surfaces (Hennequin et al 2001). It is worth noting that the smaller n=1 MHD bursts (between $t\approx9s$ and $t\approx10s$) localised in the negative shear zone of the q-profile, are mainly affecting the inner part of the barrier and have been identified as n=1 resistive interchange (Hennequin et al 2001). No MHD event is observed on the magnetic probes for the second major collapse a t=11.1s. A possible explanation arises from a careful analysis of the core impurity behaviour in these long sustained ITB discharges (Dux et al 2001). Indeed, these analyses indicate that the high-Z impurities such as Nickel accumulate in the plasma core following the neo-classical expectation and therefore steadily rise the radiative power density in the plasma center up to $140kW/m^3$: a value approaching the conducted power density. Thus the loss of confinement at 11.1s is probably a radiative collapse. The effective charge, Z_{eff}, at the plasma core rises from 2.7 ($t\approx6s$) up to 6.8 at the time of the radiative collapse when the core Nickel density provides the dominant Z_{eff} contribution (Dux et al 2001). The Z_{eff} value at mid-plasma radius (ITB

footprint) evolves from Z_{eff}=2 up to 2.6. It is worth pointing out that the two ITB collapses at 6.7s and 11.1s transiently evacuate the impurity from the core. From the analysis of the images recorded by a CCD camera showing a poloidal cross section of the JET torus, the possible source of the impurity is attributed to the interaction between the plasma and the inner wall located in the upper part of the vacuum chamber. This interaction is due to an increase of the upper triangularity at high beta while the position of the X-point is kept fixed thanks to the feedback control system (c.f. figure 12 described in the section 3). Finally, it is striking that after these major collapses the ITB recovers rapidly its characteristics. A possible interpretation for the understanding of this observed ITB robustness is put forward in the last paragraph of section 5.

The discharge shown on figure 6 is not exactly at zero loop voltage, the time average loop voltage is of the order of 0.1V corresponding to a flux consumption at the plasma boundary of 0.8Wb during the high power phase. It should be stressed that few discharges with LHCD applied in the main heating phase have also been obtained at lower plasma current (1.8MA and 1.5MA). By decreasing the plasma current, discharges with a phase of zero-loop voltage at the plasma surface or slightly negative have been obtained lasting up to 1s. For the 1.8MA discharge shown on figure 11, the negative loop voltage phase did not last longer since the LHCD power is stopped due to an automatic safety procedure that controls in real time the radiation level in the vicinity the LH grill. When the radiation level exceeds a pre-set value the LH power is stopped. The cause of the enhanced radiation level when decreasing the plasma current is not fully identified. A possible explanation is that the high energetic ions from the Hydrogen minority tail accelerated by the ICRH wave might directly interact with the LH antenna increasing the level of radiation. The minority concentration is of the order of 5%. Indeed, a lower plasma current operation increases the width of the fast ions orbit and reduces the phase space domain of the confined orbits. In the present operating condition, this is an important operational constraint when the LHCD power is applied in the main heating phase at low plasma current. The possible ways to reduce the radiation level in the vicinity of the LH antenna consists in : (i) increasing the concentration of minority Hydrogen to drive a lower energetic ions tail; (ii) and/or use He^3 minority heating; (iii) and/or to further move-back the LH antenna from the plasma boundary. These three promising routes have not been fully explored in the described experiments for a lack of experimental time.

Finally, the same type of discharge has been successfully repeated in the aim of demonstrating the feasibility of real time control of the electron temperature gradient at the ITB location in full current drive operation. The experimental details and the implementation of the feedback loops to control simultaneously the electron temperature profile and the neutron yield in this non-inductive regime are described in a companion paper (Mazon et al 2001).

3. Database analysis of the highly non-inductive current drive regime

In this section, a statistical approach is used to describe the global trend and performances of the non-inductive current drive operation. The representative discharges of such regime have been shown in section 2. We report on the analysis of 27 discharges with Internal Transport Barriers performed at the same toroidal magnetic field (B_o=3.45T) but at three different values of plasma current in the plateau phase: I_p=1.5MA ($q_{95}\approx$7.5) without LHCD in the high power phase, I_p=1.8MA ($q_{95}\approx$6.3) and I_p=2.0MA ($q_{95}\approx$5.5). The discharges selected at 1.8MA and 2MA have at least 2MW of LHCD power in the high NBI/ICRH heating phase. In this database the main plasma parameters are recorded every 150ms during the neutral beam heating phase (on average thirty times are selected per discharge). For all these experiments the LHCD power is systematically applied in the prelude phase to shape the target q-profile.

We first briefly summarise the characteristics of the magnetic equilibrium as calculated by the EFIT code constrained by the magnetic data only. The elongation, triangularities (upper and lower) at the plasma boundary and the Shafranov shift are represented versus the poloidal beta. The Shafranov shift is typically above 0.20m (one fifth of the minor radius) when the poloidal beta exceeds unity. The plasma elongation ($\approx$1.7) and the lower triangularity ($\approx$0.25) are kept at practically constant values independently of β_p. The constant values of the lower triangularity confirm that the shape controller maintains the X-point and strike point locations even when beta is increased (c.f. section 2.1). On the contrary, the upper triangularity increases from 0.12 up to 0.22 with β_p and this variation is invoked to explain the wall plasma interaction in the upper part of the vacuum chamber at high beta. The evolution of the plasma internal inductance, l_i, and loop voltage, V_s, are plotted on figure 13 (top part) versus the poloidal beta for the three values of plasma current plateau. The maximum value of β_p calculated with the diamagnetic energy content reached 1.65 at 1.5MA. The loop voltage drops to values approaching zero for β_p typically above unity. The internal inductance is kept between 0.6 and 0.9 ($0.6\leq l_i \leq 0.9$) from the low to the high beta phase, indicating that a broad current profile has been sustained when increasing the performances of the discharges. It is worth noting that for the discharges realised at I_p=1.8MA (full squares) or I_p=2MA (full circles) the internal inductance is statistically lower in the prelude phase ($\beta_p<0.6$) than for the I_p=1.5MA discharges (full triangles). This indicates that a broader or a more reversed target q-profiles were formed in the 1.8MA-2MA experiments. This is explained by the application of slightly more LHCD power (2.5MW against 3MW on average) in the current ramp-up phase for the 1.8-2MA experiments and an improvement of the plasma breakdown conditions. This global trend shown on the zero-dimensional data is in agreement with the detailed analysis of the target q-profile presented in section 2.

In terms of confinement performances, the figure of merit defined by the product of $H_{ITER89\text{-}P}$ (as revised by Kaye et al 1997) times the normalised toroidal beta β_N, is plotted versus β_p (figure 13-bottom). It should be pointed out that only the non thermal energy confinement times are available for this database

analysis. The assessment of the thermal confinement (see section 5) that relies on the detailed profile analyses generally performed with computer codes such as TRANSP (Goldston et al 1981, Budny al 1992) is carried out for a restricted number of discharges. The maximum value of the product $H_{ITER89\text{-}P}x\beta_N$ is 4.5 at β_p=1.65. For a given value of β_p, $H_{ITER89\text{-}P}x\beta_N$ reaches higher values when the plasma current is increased while the LHCD is maintained in the main heating phase. Typically at $\beta_p\approx1.0$, the product of $H_{ITER89\text{-}P}x\beta_N$ is of the order of 2.0 at I_p=1.5MA whereas it reaches 3.5 at I_p=2MA. As far as the electron density behaviour is concerned, the core electron density and the line averaged density, n_{el}, are normalised to the Greenwald density limit, $n_{Gr}=I_p/\pi a^2$ (Greenwald et al 1998), and plotted versus the improved confinement factor, HITER89-P (Figure 14a). The electron density profile is measured by the Thomson scattering diagnostic and the line integrated densities are in agreement with the interferometer measurements. The maximum value of nel/nGr is up to 0.55 at HITER89-P≈2.2 and these values are obtained both at 1.8MA and 2MA. Experiments performed at 1.5MA without LHCD in the main heating phase have the lowest performance in terms of core electron density. A similar trend is also shown on the thermal pressure in the plasma center plotted versus the central density (Figure 14b). The highest core thermal pressure is up to 140kPa obtained at high density, neo≈61019m-3 for the 1.8MA and 2.0MA experiments with LHCD in the main heating phase. A possible interpretation of this result relies on the role played by the q-profile on confinement. Indeed, the q-profile of the 1.5MA discharge discussed in section 2-1 evolves towards a weakly reversed or monotonic shape. Whereas a non-monotonic q-profile (large value of negative shear in the core) is sustained in discharges at 1.8MA-2MA with 2-3MW of LHCD power in the main heating phase. Analyses of experiments specifically devoted to illuminate the role played by the q-profile on the ITB performance have shown that a reduction of the magnetic shear down to zero or negative values could locally lead to higher core confinement with steeper pressure profiles (Challis et al 2001b, Tresset et al 2001).

As far as the H mode confinement is concerned the electron pressure has been assessed at the edge transport barrier (figure 15). The electron pedestal pressure, Pe ped, is calculated from the measurements of (i) the line averaged density using the FIR interferometer vertical chord closer to the edge transport barrier and (ii) the external measurements of the electron temperature from the ECE data. The edge pressure pedestal is represented versus the power flowing across the separatrix normalised to the L to H power threshold scaling law (Righi et al 1999, Jacquinot et al 1999). Interestingly, Pe ped are kept at low values (5 to 10 times lower than the core pressure) even at power well above the L to H threshold where type I ELMs are expected. Indeed, transition from type III to type I ELMs is expected on JET in standard H-mode regime when the power is at least twice the L to H power threshold (Sartori et al 1998). This is a important aspect in the success of the reported experiments since type I ELMs erode or degrade the performance of the ITB and do not facilitate the coupling of a large amount of LHCD powers in stationary condition (Sarazin et al 2001a). The mitigation of the ELMs in these highly non-inductive experiments has

been interpreted by analysing the role played by the broad q-profile, in particular the edge current, on the type III to type I ELM transition (Bécoulet M. et al 2001, Sarazin et al 2001b). Indeed it was found, that a larger current fraction at the plasma edge in the ITB discharges compared to the similar standard H-mode ones could prevent the type III to type I ELM transition.

4. Resistive current diffusion analysis

We report in this section on the analysis of the resistive evolution of the current profile in order to assess the residual ohmic current and the calculation of the various components of the non-inductive currents (bootstrap current, NB and LH currents) in the experiments described in section 2. Various codes have been used to analyse the neoclassical diffusion of the electric field inside the plasma with the experimental temperature and density profiles, such as ASTRA, CRONOS, JETTO and TRANSP. In this paper we describe the current diffusion simulations performed with the most recent version of the CRONOS code in which the poloidal field diffusion is solved self-consistently with the two dimensional (2-D) poloidal plane Grad-Shafranov equation (Basiuk et al 2001). The fixed boundary plasma equilibrium solver is described in (Huysmans et al 1991). The neo-classical quantities, i.e. the plasma resistivity and self-generated bootstrap current, are deduced from the NCLASS code (Houlberg et al 1997). NCLASS solves the flux-surface-averaged parallel momentum and heat-flow balance equations for each plasma species using the formulation of Hirshman and Sigmar (Hirshman and Sigmar 1981). The velocity dependent viscosity matrices are taken from a recent publication by Shaing (Shaing et al 1996) and are valid in all collisionality regimes and aspect ratios. The neo-classical bootstrap current is calculated "self-consistently" with the time varying q-profiles and the measured density and temperature profiles. The prediction of the neo-classical quantities (in particular the bootstrap current profiles) with NCLASS has been previously validated on the high bootstrap operation of Tore Supra (Saoutic et al 1994, Joffrin et al 2000). The neutral beam current has been estimated separately with the TRANSP code using a Monte-Carlo technique (Goldston et al 1981, Budny et al 1992). The LH wave propagation and absorption is calculated self-consistently with the time varying equilibrium using a ray-tracing code coupled with a two-dimensional relativistic Fokker-Planck solver (Peysson and Shoucri 1998, Imbeaux 1999, Imbeaux and Peysson 2000). Finally, it is worth pointing out that similar current diffusion simulation with CRONOS has been performed to analyse the full current drive operation sustained with Lower Hybrid current on Tore Supra (Litaudon et al 2001).

A complete current diffusion analysis is presented on figures 16 and 17 for the high poloidal beta discharge #51782 obtained at 1.5MA without LH power in main heating phase (c.f. section 2.2 and figure 2). These simulations indicate that the sum of the non-inductive currents reaches up to 82% of the total current with 0.6MA of bootstrap current and 0.65MA of NBCD. This value is reached within t=7.4s and

t=8.4s where the loop voltage is very close to zero for one second. In our time dependent simulation, the initial q-profile and poloidal flux taken at t=5s are from EFIT constrained by the MSE data. The relative time evolution of the loop voltage is in fair agreement with the experimental value. In addition, the CRONOS code simulates the Faraday and MSE polarisation angles using the calculated 2-D equilibrium quantities taking into account the precise characteristics of the two diagnostics implemented at JET (figure 16b-c). The quantitative agreement between the relative time evolution of the simulated and measured raw signals can be considered as a signature of the spatial location of the non-inductive current sources. The non-inductive driven currents at t=8s are shown on figure 17. The bootstrap current steadily rises inside a normalised radius of 0.6 where the region of steep pressure gradient is located.

Similar self-consistent calculation of the various non-inductive currents with the actual equilibrium and measured temperature profiles have been carried out for the 2MA discharge, #53521, where the LH power is maintained in the main heating phase (c.f. section 2.3 and figure 6). In the reported simulation, the initial q-profile and poloidal flux taken at t=5.1s are from EFIT constrained by the FIR polarimetry data. In addition, both the measured Carbon and Nickel impurities radial profiles have been used to reconstruct the charge effective profiles. The time traces of the various simulated quantities and their experimental counter parts are shown on figure 18. Figure 19 represents the various current density profiles at t=10.2s. At the maximum performance when the neutron yield peaks (t≈9s), the total non-inductive driven current reaches 1.85MA representing a fraction of 90% of the total plasma current. This fraction is fairly constant with time : when the electron density is increased the LH and NB non-inductive currents are both reduced but this effect is partly compensated by the rise of the bootstrap current. The simulation indicates that (i) the bootstrap current rises up to approximately 1.0MA, the NBCD varies between 0.2-0.6MA, while the LHCD deduced from ray-tracing Fokker-Planck modelling is the range 0.4-0.8MA (depending on density) corresponding to a normalised LHCD efficiency of 1.6-1.81019m-2A/W. Due to the the well localised characteristics of the ITB for this discharge, the bootstrap current peaks off-axis with a maximum value near _/_max=0.25, i.e. in the region of the steepest pressure gradients. Similarly, the LH ray-tracing simulations during the high power phase show that the LH power is absorbed in a broad off-axis region ($0.2 \leq$ _/_max ≤ 0.6) thanks to the strong electron Landau damping with high electron temperature (figure 20).

5. Local heat transport and stability analyses

The understanding of the underlying ITB physics is progressing, and it is likely that a combination of the E x B flow shear and magnetic shear play an important role in the triggering and sustainment of the ITB (e.g. Burrell 1997, Synakowski 1997, Parail 1999, Tala 2001). We evaluate in this section the role played by these quantities in the sustainment of ITB in the highly non-inductive experiments described in this

paper. We focus our analyses on the discharge #53521 (described in section 2.3, figure 6) where an ITB has been sustained during the longest duration on JET with off-axis LH current drive in the high NBI/ICRH power phase.

We first estimate the radial electric field, Er, directly from the force balance equation for the carbon (C6+) impurity:

$$E_r = (z_c e n_c)^{-1}(dp_c / dr) - V_\theta B_\phi + V_\phi B_\theta \qquad (1)$$

Where n_c, p_c, V_θ and V_ϕ are respectively the density, the thermal pressure, the poloidal, and toroidal rotation of the carbon impurity; B_θ and B_ϕ are the poloidal and toroidal component of the magnetic field. The toroidal rotation, density and temperature profiles of the carbon impurity in the plasma are measured with charge exchange spectroscopy. We have carried out our calculation when these measurements are available, i.e. during the NB heated phase. Turbulence stabilisation mechanisms in the prelude phase with LH power alone is discussed in (Hogeweij et al 2001, Conway et al 2001). We have used the neoclassical expression given by (Kim et al 1991 & 1994) to estimate the poloidal rotation velocity since there is no direct measurements of this velocity in JET. The magnetic field in particular the poloidal field, B_θ, in equation (1) is taken from EFIT constrained by the polarimetry data (the corresponding q-profiles are shown on figure 9). The electric field is up to 55kV/m just inside the ITB and the main contribution to E_r comes from the toroidal rotation component (figure 20). The expression for the $\boldsymbol{E}$ x $\boldsymbol{B}$ shearing rate, $\gamma_{E\times B}$, is calculated by taking the radial derivative of the toroidal angular speed, E_r/RB_θ, due to the equilibrium flow driven by E_r as (Waltz et al 1997, Burrel et al 1997):

$$\gamma_{E\times B} = \left| \frac{RB_\theta}{B} \frac{\partial}{\partial r}\left(\frac{E_r}{RB_\theta} \right) \right| \qquad (2)$$

where r is the minor radius in the outer mid-plane. The toroidal angular speed E_r/RB_θ, shown on figure 20 at different times during the high power phase has a significant derivative at R=3.5m close to the ITB footpoint, and rise up to 160×10^3rad/s. Consequently the maximum value of the $\boldsymbol{E}$ x $\boldsymbol{B}$ shear flow, $\gamma_{E\times B}$, stays locally in excess of the growth rate for the toroidal branch of the ion temperature gradients (ITG) driven instability, γ_{ITG}, as quantitatively shown on figure 21. Non-linear simulations of the ITG modes have shown turbulence stabilisation when $\gamma_{E\times B}$ is comparable or exceeds the maximum linear growth rate of the modes (Waltz et al 1994, Waltz et al 1995). For the figure 21, a simplified analytical expression for γ_{ITG} has been used (Newman et al 1998, Crisanti et al 2001) but including the magnetic shear effect on the ITG growth rate (Esposito et al 2001). The magnetic shear dependence has been derived by fitting the

numerical simulations of the ITG turbulence obtained with gyrofluid and gyrokinetic codes (Waltz et al 1997). A high value of $\gamma_{E\times B}$ exceeding γ_{ITG} is maintained throughout the main heating phase. In this phase, the ion thermal diffusivity inside the ITB is reduced down to 0.4-0.5m^2/s as calculated by TRANSP using the measured thermal pressure profiles. The various radial profiles of these quantities are plotted on figure 22 at t=10.5s. The $\boldsymbol{E}$ x $\boldsymbol{B}$ shearing rate exceeds the maximum value of the ITG growth rate at the plasma boundary (the edge transport barrier) and at mid plasma radius where the core transport barrier is located. The thermal electron and ion thermal diffusivities drop significantly in the core region by a factor of 10 within 15cm (inside $3.4m \leq R \leq 3.55m$), precisely where the $\gamma_{E\times B}$ is in excess of the ITG growth rate.

In addition, we have also evaluated the linear growth rates of the plasma microinstabilities using the electrostatic linear gyrokinetic code, KINEZERO (Bourdelle et al 2000, 2001). The profiles used as inputs in KINEZERO are the measured temperatures, densities and q-profiles. In the current version of the code, the Shafranov shift effect is implemented in the framework of the 's-α' model ($\alpha=-q^2R d\beta/dr$) with shifted circles magnetic surfaces (Connor et al 1978). The purpose of the reported study is to investigate numerically the relative role of the q-profile in sustaining the ITB. Figure 23 shows the results of two simulations where only the q-profile has been varied. In the first similation (full line) we have ran KINEZERO with the measured non-monotonic q-profile as inferred from EFIT constrained by the polarimetry data. We have plotted the linear growth rates for the low wavenumbers modes (such as $k_\theta \rho_i \leq 1$ where ρ_i is the ion Larmor radius and k_θ the poloidal wavenumber) where the ion instabilities driven by the ITG and the trapped electron modes (TEMS) are dominant. This simulation indicates that these modes are suppressed in the region of low magnetic shear at mid-plasma radius. A similar calculation has been repeated keeping the same experimental temperature profiles but varying only the q-profile from a non-monotonic shape to a monotonic one, i.e. varying the magnetic shear from the actual measured values to 0.5. With a monotonic q-profile these low wavenumber modes at mid-plasma radius are destabilised (figure 23, dashed line). We confirm by this linear stability analysis that the q-profile and its shear play an important role in reducing the growth rates of the ion modes. By maintaining with non-inductive means the non-monotonic q-profile we act directly on the growth rate of these modes. One of the surprising result of this experiment is that the ITB is reformed immediately after major perturbations or collapses as discussed in section 2.3. These collapses affect on a fast time scale the pressure, toroidal rotation and radial electric field profiles but the q-profile, evolving on a longer time scale, keeps a non-monotonic shape. Therefore, the direct reduction or stabilisation of the turbulence through the q-profile could be invoked to explain the rapid recovery of the ITB to various perturbations such as MHD or radiative core collapses as long as these perturbations weakly affect the low or negative magnetic shear region ($\rho/\rho_{max} \approx$ 0.4-0.5). Finally, it should be stressed that when the ITB is fully developed, the linear growth rates in the

steep pressure gradient zone ($\rho/\rho_{max} \approx 0.2$-$0.4$) are also significantly reduced by the Shafranov shift stabilisation effect with the α-parameter reaching up to 2.5.

6. Conclusion and prospects

We have reported on the successful highly non-inductive current drive operation on JET where improved confinement regime characterised by a significant reduction of the anomalous transport in the plasma core is maintained on a duration much larger than the energy confinement time ($\approx 37\tau_E$) and already approaching a current resistive time. Thanks to a high fraction of non-inductive current (above 80%) internal transport barrier is sustained during up to 11s which is the longest duration of sustainment of this regime on JET. The duration of the discharges is close to the technical operational limits fixed by the maximum duration of (i) the application of the full NBI power and (ii) the high toroidal field operation (B_o=3.45T). The resistive evolution of the target q-profile formed during the initial lower hybrid assisted current ramp-up phase is slow down even when the plasma current plateau is reached due to a favourable combination of bootstrap, neutral beam and LH current. We have investigated two series of experiments at reduced plasma current ($q_{95} \geq 5.5$) with or without lower hybrid current during the main heating phase. In these experiments where the fraction of non-inductive current driven by the neoclassical bootstrap effect is in the range of 50% (up to 1.0MA), the off-axis LH current plays a major role in maintaining the broad current profile. In particular, we have developed regime where the target q-profile (measured at a time just prior to the main heating phase) has a minimum q value above two at typically mid radius. In the experiments where the LH power is applied during the main heating phase, the q-profile is maintained above two while keeping a non-monotonic shape. It should be stressed that the mild ELMs activity (type III ELMs) observed in these experiments is a key aspect in the success of this highly non-inductive operation. Indeed, the grassy ELMs activity facilitates the coupling of the ICRH and LHCD systems and, more fundamentally, prevents the erosion or degradation of the core transport barrier induced by large MHD activity triggered at the plasma edge (e.g. triggered by type I ELMs). It has been suggested that the avoidance of the type I ELM could be explained by the large edge current fraction in regimes with broad current profile characterised by low internal inductance (Bécoulet M. 2001, Sarazin et al 2001b). This is an important result for steady state tokamak operation since by maintaining a broad current profile by non-inductive means one could simultaneously sustain a core transport barrier and mitigate the ELM activity.

Despite these favourable results for advanced steady state tokamak operation, many other important aspects remain to be explored before extrapolating this regime to the next step device such as ITER as thoroughly discussed by Bécoulet A. et al (2001). In particular, one has to develop similar quasi steady state regime in highly shape plasma at higher triangularity in the range of 0.5 as requested in the present ITER design. The issue of the compatibility of the ITB performance at high triangularity has to be

addressed. Performances in terms of normalised pressure (e.g. β_N) and confinement should be further increased by extending the width of the ITB. Indeed, previous ideal MHD calculation by Bondesson et al (1999) has shown that the limit to the normalised beta could be further increased (up to 3.8 with a conducting wall) in particular when $q_{min} \approx 2.2$. Exploring experimentally the beta limits in this highly non-inductive operation is an open issue. In the described experiments the line averaged density normalised to the Greenwald limit is up to 0.55. Therefore, exploring stationary regime at higher normalised density should also be investigated. The edge condition of the ITB regime should be compatible with good plasma exhaust. Effort should be pursued to increase the edge density taking advantage of the long duration of the discharge while keeping a mild ELM activity. Finally, study of the impurity behaviour in these long duration discharges has shown that the impurities follow a neo-classical behaviour and accumulate in the core of the plasma. Control of the impurity accumulation should be investigated either by triggering core MHD activity or by controlling the density and temperature profiles. Indeed, on the real time control aspect of the ITB a major step has been made by controlling the local electron temperature gradient in this highly non-inductive regime (Mazon et al 2001). This effort will be pursued by taking advantage in the near future of the real time information of the electron density, ion temperature and q-profiles. In particular, these developments should be gear to achieve a better control of the ITB's characteristics (location, strenght...) and impurity contents. The answers to these important issues, briefly recalled in this conclusion, are required to better extrapolate this stationary regime to the next step device and these aspects will be investigated in the future experimental campaigns on JET.

Acknowledgement

This work has been performed under the European Fusion Development Agreement (EFDA). It is a pleasure to acknowledge the contributors to the EFDA-JET work programme, the UKAEA, operator of the EFDA-JET facility, and the EFDA Close Support Unit in Culham.

References

Alladio F. et al. 2000 In Fusion Energy (Proc. 18th Int. Conf. Sorrento, 2000) IAEA, Vienna

Baranov Yu. F. et al 1999 Nucl. Fus. **39** 1463

Basiuk V. et al 2001 proc. of the Transport Task Force meeting (Fairbank, USA, 2001)

Becoulet A. et al 2001 accepted in Plasma Physics and Control. Fusion

Becoulet M. et al 2001 submitted to Plasma Physics and Control. Fusion; Controlled Fusion and Plasma Physics (Proc. 28th Eur. Conf. Madeira, 2001) (European Physical Society)

Bondesson A., Liu D.H., Söldner F.X., Persson M., Baranov Yu F., Huysmans G.T.A. Nucl. Fusion 1999 **39** 1524

Bourdelle C, Garbet X., Maget P., Hoang G.T., Monier-Garbet P. in Controlled Fusion and Plasma Physics (Proc. 27th Eur. Conf. Budapest, 2000) vol 24B (European Physical Society) p 1092

Bourdelle C, X. Garbet, Hoang G.T., Ongena, J. Budny R.V. sumitted to nuclear Fusion

Budny R.V. et al 1992 Nucl. Fusion **32** 429

Burrel K.H. 1997 Phys. Plasmas **4** 1499

Challis C.D. et al 2001a Plasma Physics and Control. Fusion **43** 861

Challis C.D. et al 2001b in Controlled Fusion and Plasma Physics (Proc. 28th Eur. Conf. Madeira, 2001) (European Physical Society)

Connor J.W, Hastie R.J., Taylor J.B. 1978 Phys. Rev. Letter **40** 396

Conway G.D. et al 2001 in Controlled Fusion and Plasma Physics (Proc. 28th Eur. Conf. Madeira, 2001) (European Physical Society)

Crisanti F. et al Nucl. Fusion 2001 **41** 883

Crisanti F. et al 2001 submitted to Phys. Rev. Letters

Dux R. et al 2001 in Controlled Fusion and Plasma Physics (Proc. 28th Eur. Conf. Madeira, 2001) (European Physical Society)

Equipe Tore Supra (presented by X. Litaudon) 1996 Plasma Phys. Control. Fusion **38** A251

Esposito et al 2001 in Controlled Fusion and Plasma Physics (Proc. 28th Eur. Conf. Madeira, 2001) (European Physical Society)

Fuchs et al 2000 in Controlled Fusion and Plasma Physics (Proc. 27th Eur. Conf. Budapest, 2000) vol 24B (European Physical Society) p 1084

Goldston R.J. et al 1981 J. Computer Phys. **43** 61

Gormezano C. 1999 Plasma Phys. Control. Fusion **41** B367

Gormezano C. 2000 in Controlled Fusion and Plasma Physics (Proc. 27th Eur. Conf. Budapest, 2000) vol 24B (European Physical Society) p 245

Greenwald et al M. 1988 Nucl. Fusion **28** 2199

Hawkes N. et al 2001a Phys. Rev. Lett. **87** 115001

Hawkes N. et al 2001b submitted to Plasma Phys. Control. Fusion

Hawkes N.C., Blackler K., Viaccoz B., Wilson C. H., Migozzi J.B. and Stratton B.C. 1999 Rev. Sci. Instrum. **70** 894

Hoang G.T. et al 2000 Phys. Rev. Lett. **84** 4593

Hogeweij G.M.D. et al 2001 in Controlled Fusion and Plasma Physics (Proc. 28th Eur. Conf. Madeira, 2001) (European Physical Society)

Hender T.C. et al 1999 in Controlled Fusion and Plasma Physics (Proc. 26th Eur. Conf. Maastricht, 1999) vol 23J (European Physical Society) p89

Hennequin P. et al 2001 in Controlled Fusion and Plasma Physics (Proc. 28th Eur. Conf. Madeira, 2001) (European Physical Society)

Hirshman S.P. and Sigmar D.J. 1981 Nucl. Fusion **21** 1079

Houlberg W. A. et al 1997 Phys. Plasmas **4** 3230

Huysmans G.T.A., Goedbloed J.P. and Kerner W., 1991 CP90 Conference on Comp. Physics, World Scientific Publ. Co. 371

Huysmans G.T.A., Hawkes N.C., Hender T. C. and Litaudon X. 2001 to be published in Phys. Rev. Lett.

Ide S., Fujita T., Naito O. and Seki M. 1996 Plasma Phys. Control. Fusion **38** 1645

Imbeaux F. 1999, *Etude de la propagation et de l'absorption de l'onde hybride dans un plasma de tokamak par tomographie X à haute énergie*, Rep Eur-CEA-FC-1679, Association EURATOM-CEA, CEA-Cadarache

Imbeaux F. and Peysson Y. 2000 Phys. Rev. Lett. **84** 2873

Ishida S. et al 1997 Phys. Rev. Lett **79** 3917

JET Team (presented by C. Gormezano) 1999 Nuc. Fusion **39** 1875

Jacquinot J. et al 1999 Nucl. Fusion **39** 235

Joffrin E., Basiuk V., Bregeon R., Litaudon X. 2000 Plasma Phys. and Control. Fusion **42** 1227

Kamada Y. 2000 Plasma Phys. Control. Fusion **42** A65

Kaye S.M. et al 1997 Nucl. Fus. **37** 1303

Kessel C.E. Nuc. Fusion 1994 1221

Kikuchi M 1990 Nucl. Fusion **30** 265

Kikuchi et al 2001to be published in Plasma Phys. Control. Fusion

Kim Y.B., Diamond P.H. and Groebner R.J. 1991 Phys. Fluids B **3** 2050

Kim Y.B. et al 1994 Phys Rev. Lett. **72** 2199

Lao L.L., Ferron J.R., Groebner R.J., Howl W., St John H., Strait E.J., Taylor T.S. 1990 Nuc. Fusion **30** 1035.

Levinton F.M. et al 1995 Phys. Rev. Lett **75** 4417

Litaudon 1998 Plasma Phys. Control. Fusion **40** A251

Litaudon X. et al 2000, *Profile control studies for JET optimised shear regime*, Rep Eur-CEA-FC-1693, Association EURATOM-CEA, CEA-Cadarache

Litaudon X. et al 2001 Plasma Phys. Control. Fusion **43** 677

Mazon D. et al 2001 in Controlled Fusion and Plasma Physics (Proc. 28th Eur. Conf. Madeira, 2001) (European Physical Society)

Newman D.E. et al 1998 Phys. Plasmas **5** 938

Peysson Y. and Shoucri M. 1998 Comp. Phys. Comm. **109** 55

Rebut P.H., Boucher D., Gormezano G., Keen B.E. and Watkins M.L. 1993 Plasma Phys. Control. Fusion **35** A3

Saoutic B. et al 1994 Plasma Phys. Control. Fusion **36** B123

Sarazin Y. et al 2001a Controlled Fusion and Plasma Physics (Proc. 28th Eur. Conf. Madeira, 2001) (European Physical Society)

Sarazin Y. et al 2001b submitted to Plasma Phys. Control. Fusion

Sartori R. et al 1999 in Controlled Fusion and Plasma Physics (Proc. 26th Eur. Conf. Maastricht, 1999) vol 23J (European Physical Society) p 197

Strait E. J. et al 1995 Phys. Rev. Lett **75** 4421

Synakowski E.J. 1998 Plasma Phys. Control. Fusion **40** 581

Parail V.V. et al 1999 Nucl. Fusion **39** 429

Söldner F.X. et al 1999 Nucl. Fusion **39** 407

Shaing K.C., Yokoyama M., Wakatani M., Hsu C.T., 1996 Phys. Plasmas **3** 965

Sips A.A.C. et al 1998 Plasma Phys. Control. Fusion **40** 1171

Synakowski E.J. et al 1998 Plasma Phys. Control. Fusion **40** 581

Righi E. et al 1999 Nucl. Fusion **39** 309

Tala T.J.J. et al 2000 Nucl. Fusion **40** 1635

Tala T.J.J., Heikkinen J.A., Parail V.V., Baranov Yu. F. and Karttunen S.J. 2001 Plasma Phys. Control. Fusion **43** 507

Taylor T.S. 1997 Plasma Phys. Control. Fusion **39** B47

Tuccillo A. et al 2001 to be published in Radiofrequency Power in Plasmas (Proc. 14th Top. Conf. on RF Power in Plasmas, Oxnard 2001), American Institute of Physics, New York

Tresset G. et al 2001 in Controlled Fusion and Plasma Physics (Proc. 28th Eur. Conf. Madeira, 2001) (European Physical Society) and to be published in Nuclear Fusion

Waltz R.E., Kerbel G.D. and Milovich J. (1994) Phys. Plasma **1** 2229

Waltz R.E., Kerbel G.D., Milovich J. and Hammet G.W. (1995) Phys. Plasma **2** 2408

Waltz R.E., Staebler G.M., Dorland W. et al 1997 Phys. Plasmas **4** 2482

Wolf R.C. et al 1999 Plasma Phys. Control. Fusion **35** B93

Figure caption

Figure 1. JET vacuum vessel with the Gas Box divertor and the contour plots of the flux surfaces for two discharges with Internal Transport Barriers but at different poloidal beta. The dashed lines corresponds to the discharge #51726 at β_p=0.65 (I_p=3.1MA, B_o=3.4T) while the full line corresponds to the discharge #51782 at β_p=1.65 (I_p=1.5MA, B_o=3.4T).

Figure 2. Time evolution of the main parameters of a highly non-inductive discharge (#51782): LHCD power (P_{LHCD}), plasma current (I_p), NBI (P_{NBI}), ICRH powers (P_{ICRH}), neutron yield (R_{nt}), central ion (T_{io}) and electron temperature (T_{eo}), central electron density (n_{eo}), D_α emission, internal inductance (l_i) and plasma surface voltage (V_s).

Figure 3. Long lived tearing modes activity preventing the formation of an Internal Transport Barrier at 1.5MA (#51780). Time evolution of the applied power, neutron rate, amplitude of the n=1 MHD activity, and spectrogram of the pick-up coils signals. The dashed line corresponds to the time traces of the discharge shown on figure 2 where an ITB is formed (#51782).

Figure 4. Target q-profile from EFIT constrained by the MSE data for the discharge shown on figure 2 (full line, #51782) and on figure 3 (dashed line, #51780). The location of the m/n=3/1 island preventing the ITB formation is also shown for the discharge #51780. The effect of the plasma radial electric field on the MSE measurements is corrected. The q-profile is plotted versus the normalised square root of the toroidal flux.

Figure 5. (top) Toroidal rotation profiles, V_ϕ, from CXS measurements; (bottom) q-profile evolution from polarimetry data (#51782). The plasmas profiles are plotted versus the normalised square root of the toroidal flux.

Figure 6. Time evolution of the main parameters of a highly non-inductive discharge (#53521): LHCD power (P_{LHCD}), plasma current (I_p), NBI (P_{NBI}), ICRH powers (P_{ICRH}), neutron yield (R_{nt}), central ion (T_{io}) and electron temperature (T_{eo}), central electron density (n_{eo}), D_α emission, internal inductance (l_i) and plasma surface voltage (V_s).

Figure 7. Radial profiles of the ion temperature (T_i), toroidal rotation (V_ϕ), electron temperature (T_e), and electron density (n_e) at various times for the discharge shown on figure 6 (#53521). The plasmas profiles are plotted versus the major radius.

Figure 8. Variation of the target q-profile by changing the time of application of the full NBI and ICRH powers or the level of LHCD power in the current ramp-up phase (pre-heating phase). With 2.9MW of LHCD power during the current ramp-up phase, the target time is varied from t=5s (open squares, #53686), t=4.2s (open triangles, #53521) and t=3.7s (open circles, #53680). At t=3.7s, the LH power in the ramp-up phase has been decreased down to 1MW (full line, #53681). The q-profiles are deduced from EFIT constrained by MSE data and are plotted versus the normalised square root of the toroidal flux.

Figure 9. q-profiles for the highly non-inductive discharge shown on figure 6 : (top) target q-profile from EFIT constrained either by the MSE or the far Infra-Red polarimetry data; (bottom) q-profile evolution deduced from EFIT constrained by the far Infra-red polarimetry measurements (#53521). The q-profiles are plotted versus the normalised square root of the toroidal flux.

Figure 10. (top) Space-time evolution the electron temperature barrier, radial position of the q_{min} surface and n=1 MHD activity; (bottom) time evolution of the central density of the high-Z metallic impurity (Nickel) (#53521). For the top figure the normalised radius is the square root of the toroidal flux.

Figure 11. Time evolution of a I_p=1.8MA discharge with a negative loop voltage phase (#53698). LHCD power (P_{LHCD}), plasma current (I_p), NBI (P_{NBI}), ICRH powers (P_{ICRH}), central ion (T_{io}) and electron temperature (T_{eo}), central electron density (n_{eo}), D_α emission, internal inductance (l_i) and plasma surface voltage (V_s).

Figure 12. Magnetic configuration of the highly non-inductive discharges : Shafranov shift, elongation, upper and lower triangularity at the plasma boundary versus the poloidal beta. The magnetic data are deduced from the EFIT code constrained by magnetic data only.

Figure 13. Plasma performances of the highly non-inductive discharges obtained at a plasma current of respectively 1.5MA, 1.8MA and 2.0MA: (top) the product $H_{ITER89\,P} x\, \beta_p$ versus the poloidal beta, β_p; (bottom) plasma internal inductance, l_i, and loop voltage, V_s, versus β_p.

Figure 14. Electron density of the highly non-inductive discharges obtained at a plasma current of respectively 1.5MA, 1.8MA and 2.0MA. (14-a) Central and line averaged electron density normalised to the Greenwald density versus the improved confinement factor, $H_{ITER89\,P}$. (14-b) Central thermal pressure versus the central electron density.

Figure 15. Electron pressure pedestal versus the power crossing the scrape off layer normalised to the power threshold for an L to H-mode transition. The data corresponds to the highly non-inductive discharges obtained at a plasma current of respectively 1.5MA, 1.8MA and 2.0MA

Figure 16. Current diffusion simulation with CRONOS of the discharge #51782 shown on figure 2. (16-a) Time evolution of the bootstrap current ($I_{Boot.}$), neutral beam current (I_{NBCD}), LH current (I_{LHCD}) and the sum of the non-inductive driven current (I_{NI}); time evolution of the measured (dashed line) and simulated (full line) loop voltage at the plasma surface, Faraday rotation angles for three different line of sights and MSE polarisation angles at R=3.1m, R=3.25m, R=3.4m. For the sake of the clarity of the figure, the time evolution of the Faraday angles of only three representative chords has been plotted. Similar agreement is obtained with the other chords. (16-b) Measured and simulated MSE polarisation angles at t=7s. (16-c) Measured and simulated Faraday rotation angles at t=8s for each line of sight (the line of sight #1 was not in operation). The poloidal cross section of JET with the corresponding height line of sights of the FIR polarimetry diagnostic is also shown.

Figure 17. Current diffusion simulation with CRONOS of the discharge #51782. The density profiles of the of the bootstrap, neutral beam and total currents at t=8s.

Figure 18. Current diffusion simulation with CRONOS of the discharge #53521 shown on figure 6. (18-a) Time evolution of the bootstrap current ($I_{Boot.}$), neutral beam current (I_{NBCD}), LH current (I_{LHCD}) and the sum of the non-inductive driven current (I_{NI}); time evolution of the measured (dashed line) and simulated (full line) evolution of the loop voltage, internal inductance, Faraday rotation angles for three different line of sights. For the sake of the clarity of the figure, the time evolution of the Faraday angles of only three representative chords has been plotted. Similar agreement is obtained with the other chords. (18-b) Measured and simulated MSE polarisation angles at t=5.5s. (18-c) Measured and simulated Faraday rotation angles at t=10.2s for each line of sight (the line of sight #1 and #4 were not in operation).

Figure 19. Current diffusion simulation with CRONOS of the discharge #53521. The density profile of the bootstrap, LH, neutral beam and total at t= 10.2s.

Figure 20. (a) Reconstructed radial electric field profile, E_r, for #53521 (full line and open circles). The contributions from the different components in the radial electric field equation are also indicated. (b) E_r/RB_θ radial profiles at different times (t=5s, t=8s, t=11s) during the high power NBI heated phase. The error bars represent the standard deviation when the parameters that go into the calculations are varied randomly within their margins of error.

Figure 21. (top) Time evolution of the maximum value across plasma radius of the E x B shearing rate, $\gamma_{E\,x\,B}$, and the linear growth rate of the ITG modes, γ_{ITG}, evaluated where $\gamma_{E\,x\,B}$ is maximum. (bottom) Time evolution of the ion thermal diffusivity from TRANSP just inside the ITB (R=3.4m, full line) and at the footpoint of the ITB (R=3.55m, dashed line). (pulse #53521)

Figure 22. (top) Radial profile of the ExB shearing rate, $\gamma_{E\,x\,B}$, (full line) and ITG linear growth rate, γ_{ITG}, (dashed line) at t=10.5s. (bottom) Radial profile of the ion (full line) and electron (dashed line) thermal diffusivities (resp. χ_i and χ_e) at t=10.5s. The grey area corresponds to the core region where the ExB shearing rate exceeds the ITG linear growth rate (pulse #53521).

Figure 23. Linear growth rates, γ, obtained by the gyrokinetic code KINEZERO for low wavenumbers such as $k_\theta \rho_i \leq 1$. The full line corresponds to the simulation performed with the measured q-profile (pulse #53521 at t=10.5s). The dashed line corresponds to a monotonic q-profile case with positive magnetic shear.

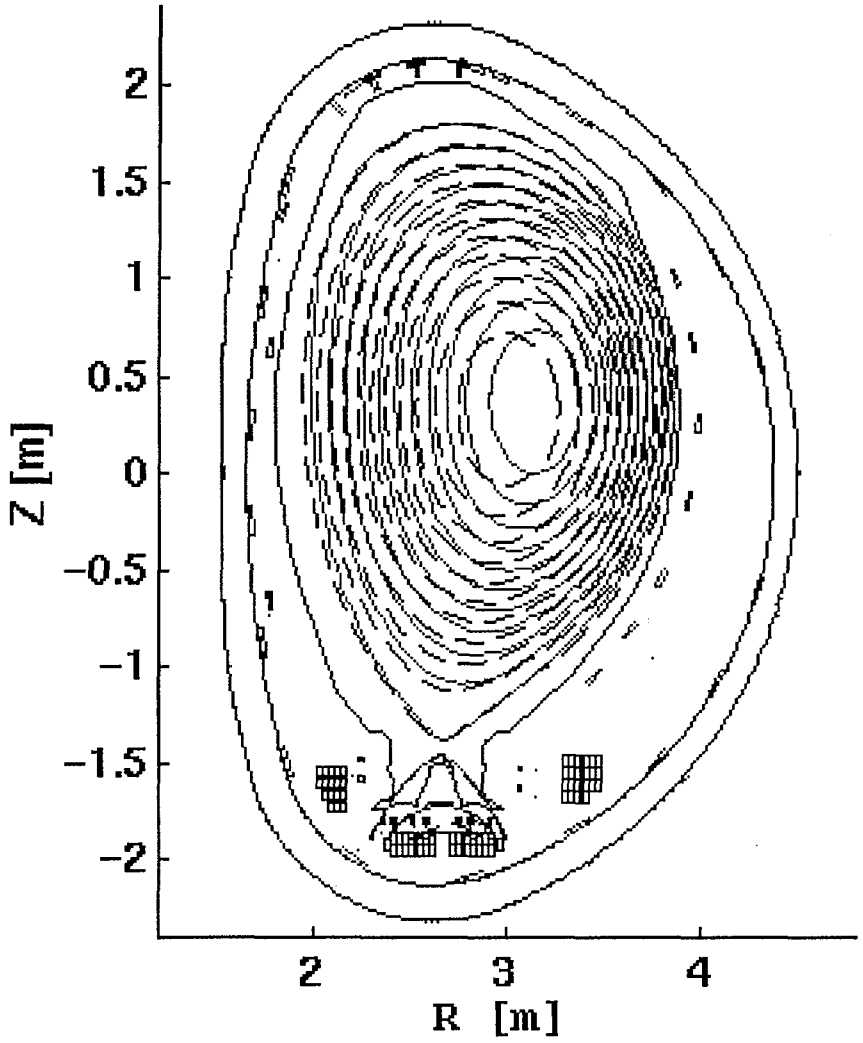

Figure 1

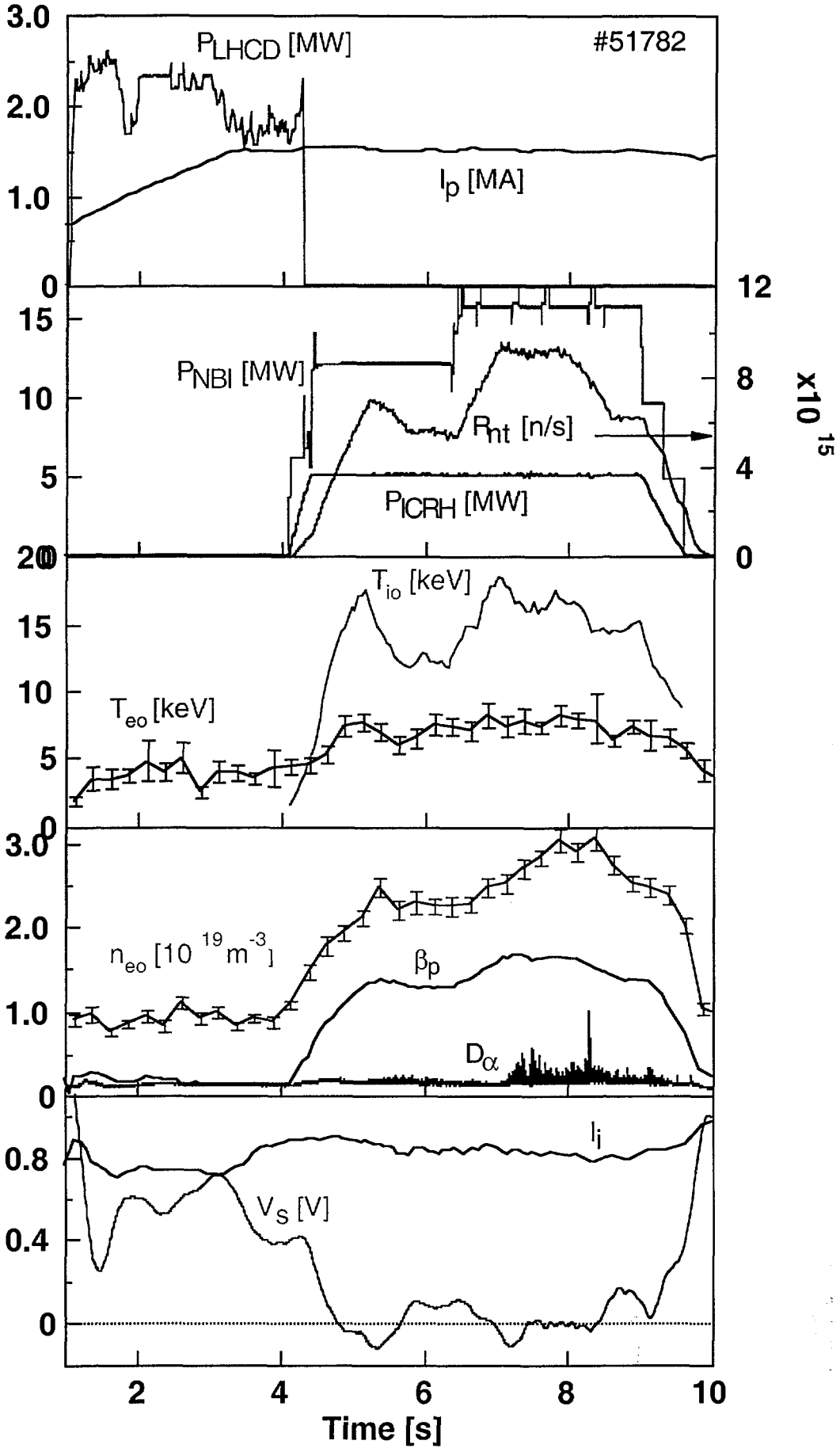
3.0
2.0
1.0
0
P_{LHCD} [MW]
#51782
I_p [MA]
15
10
5
0
P_{NBI} [MW]
R_{nt} [n/s]
P_{ICRH} [MW]
12
8
4
0
x10 15
T_{io} [keV]
T_{eo} [keV]
n_{eo} [10 19 m-3]
β_p
D_α
l_i
0.8
0.4
V_S [V]
2
4
6
8
10
Time [s]

Figure 2

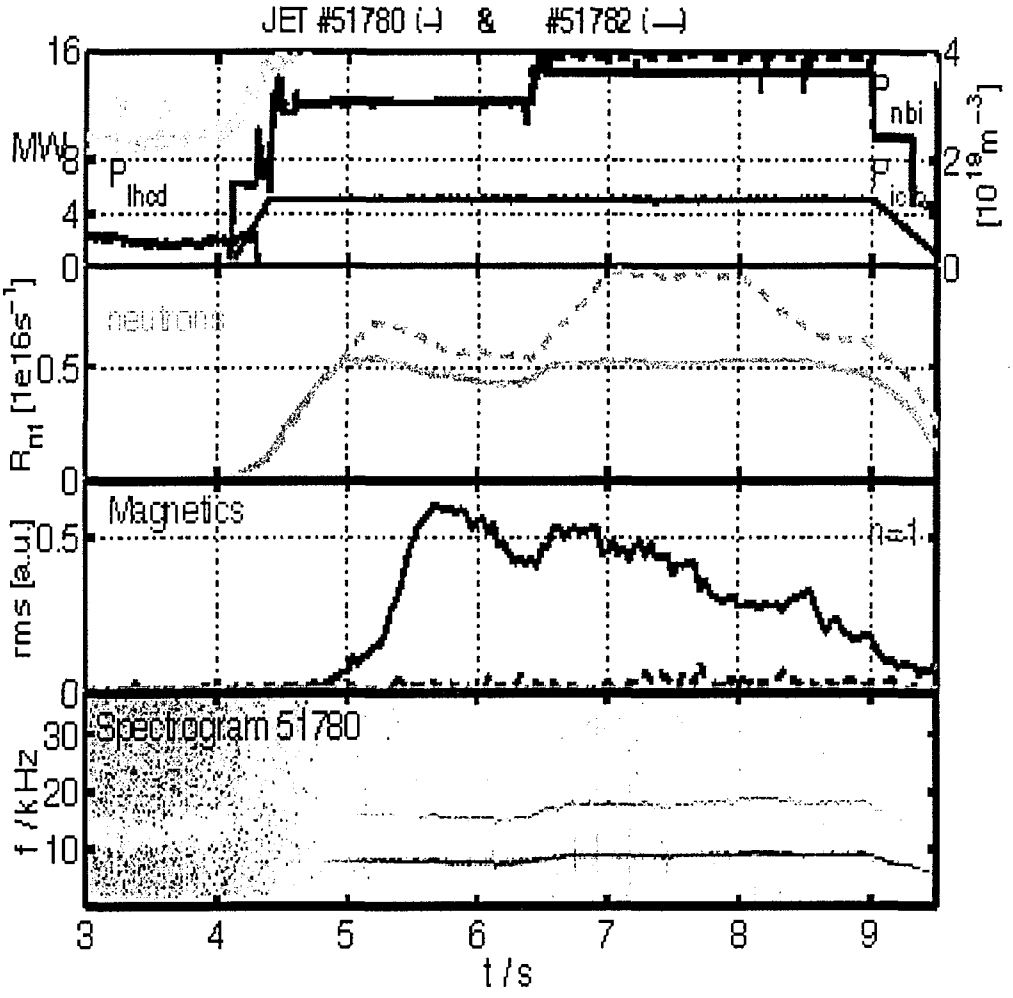
JET #51780 (-) & #51782 (—)
MW
P lhcd
P nbi
P icrh
[10^19 m^-3]
neutrons
R_n1 [1e16s^-1]
Magnetics
rms [a.u.]
n=1
Spectrogram 51780
f / kHz
t / s

Figure 3

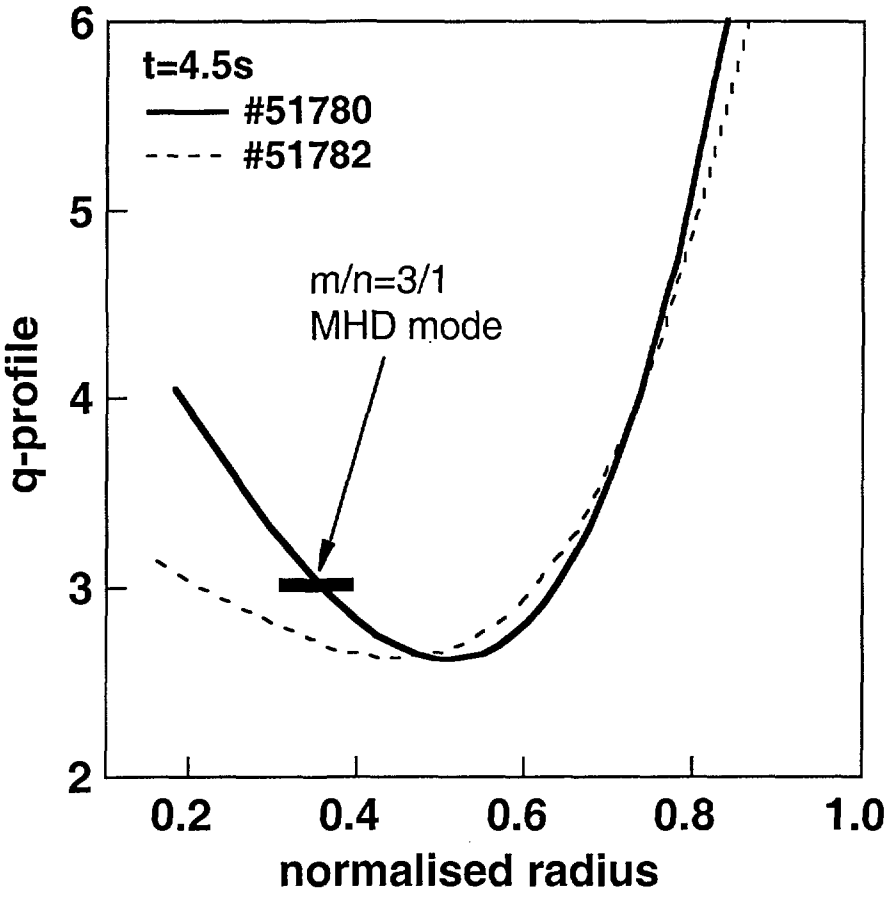
t=4.5s
#51780
#51782
m/n=3/1
MHD mode
q-profile
6
5
4
3
2
0.2
0.4
0.6
0.8
1.0
normalised radius

Figure 4

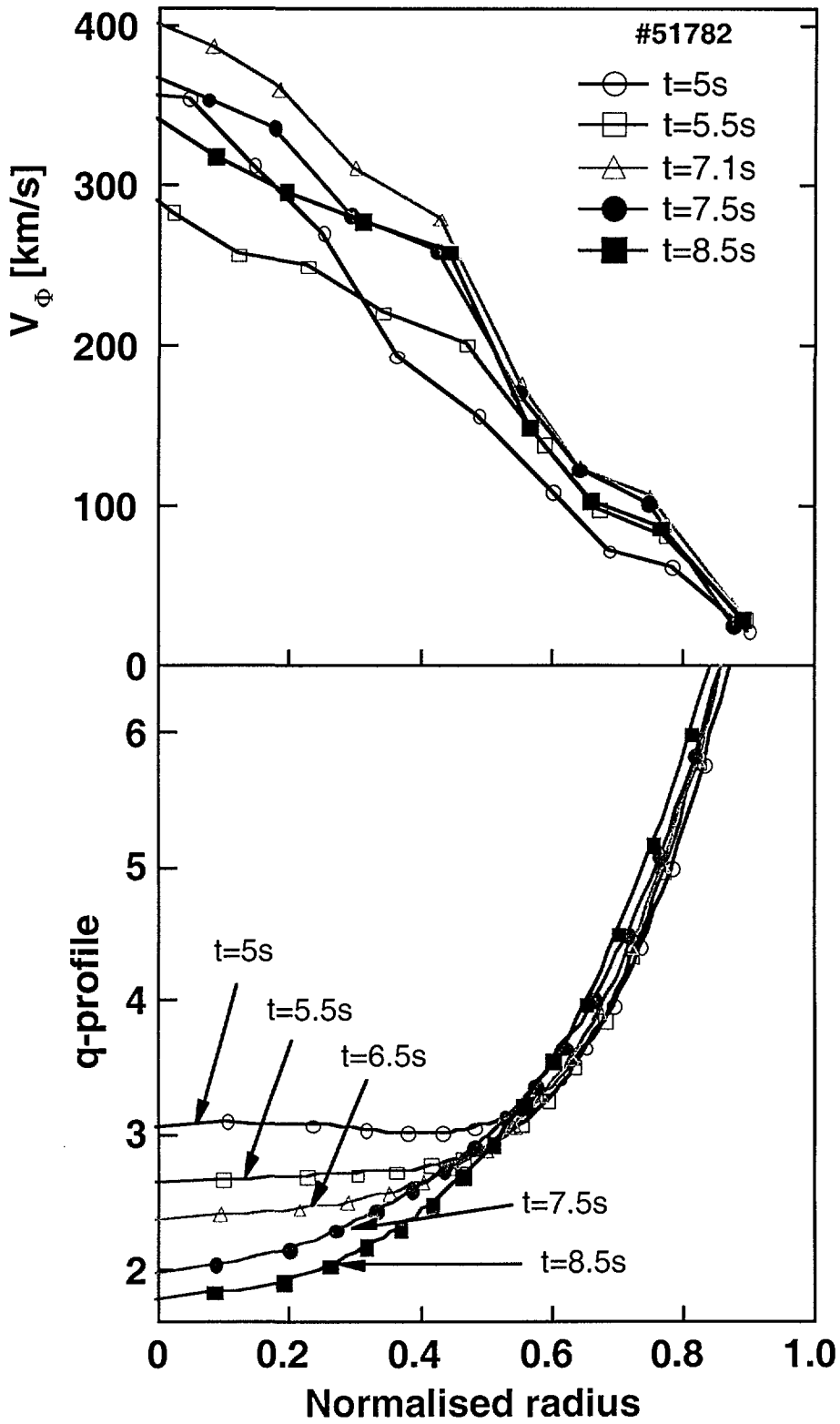
#51782
t=5s
t=5.5s
t=7.1s
t=7.5s
t=8.5s
V_Φ [km/s]
400
300
200
100
0
q-profile
6
5
4
3
2
t=5s
t=5.5s
t=6.5s
t=7.5s
t=8.5s
0
0.2
0.4
0.6
0.8
1.0
Normalised radius

Figure 5

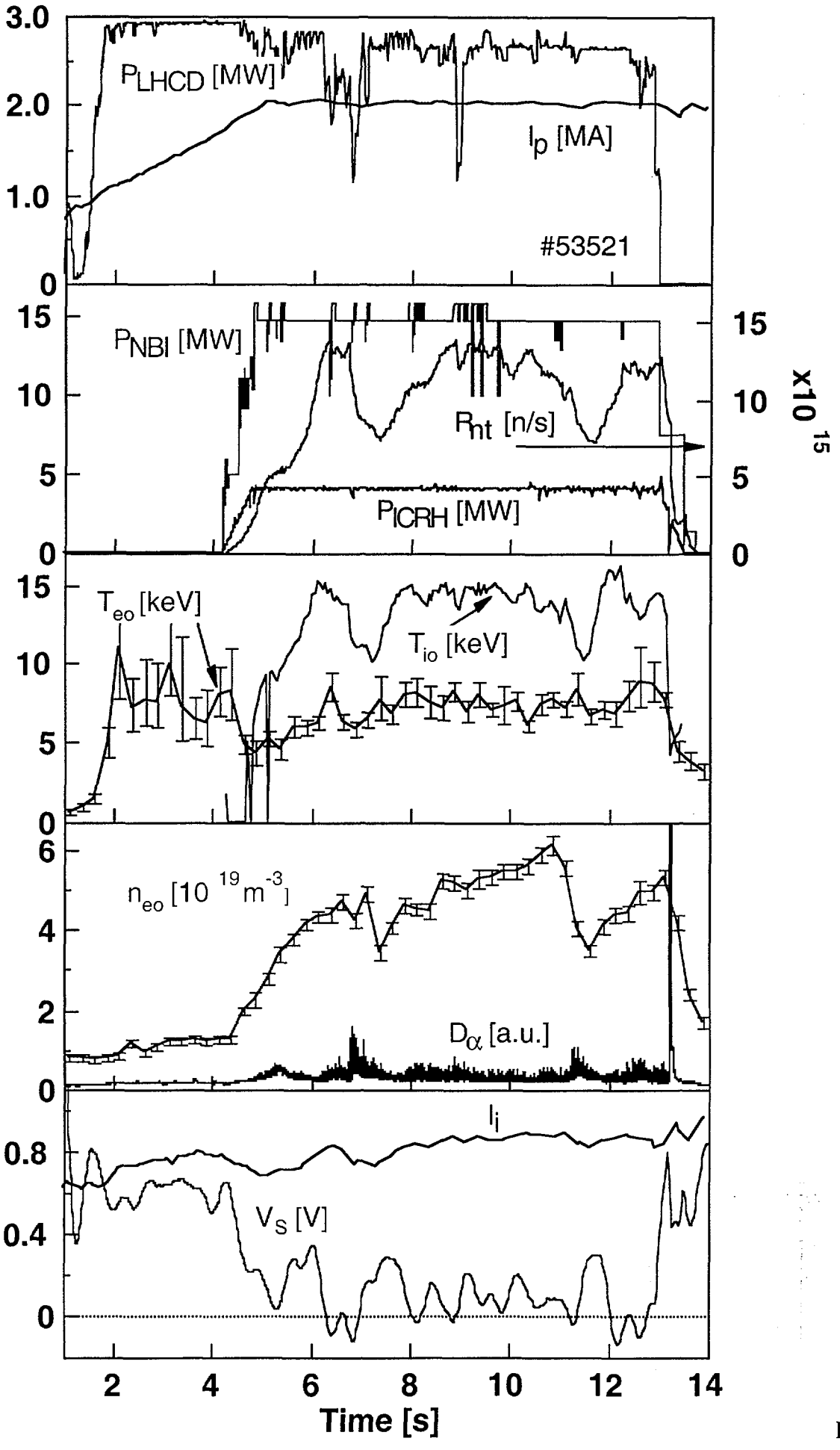
3.0
2.0
1.0
0
P_{LHCD} [MW]
I_p [MA]
#53521
15
10
5
0
P_{NBI} [MW]
R_{nt} [n/s]
P_{ICRH} [MW]
15
10
5
0
x10 15
15
10
5
0
T_{eo} [keV]
T_{io} [keV]
6
4
2
0
n_{eo} [10^{19} m^{-3}]
D_α [a.u.]
l_i
0.8
0.4
0
V_S [V]
2
4
6
8
10
12
14
Time [s]

Figure 6

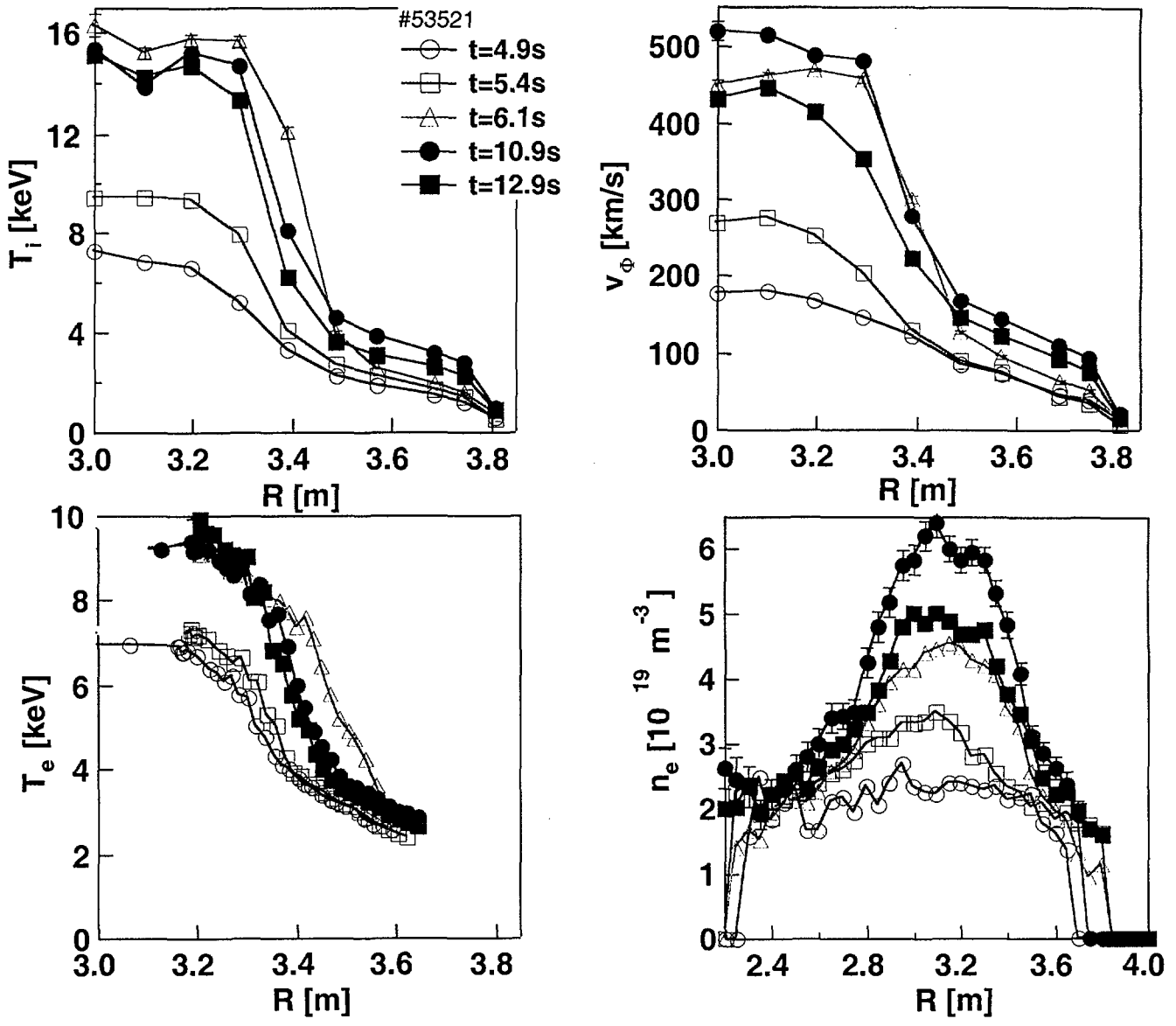
#53521
t=4.9s
t=5.4s
t=6.1s
t=10.9s
t=12.9s
T_i [keV]
v_ϕ [km/s]
T_e [keV]
n_e [10^{19} m^{-3}]
R [m]

Figure 7

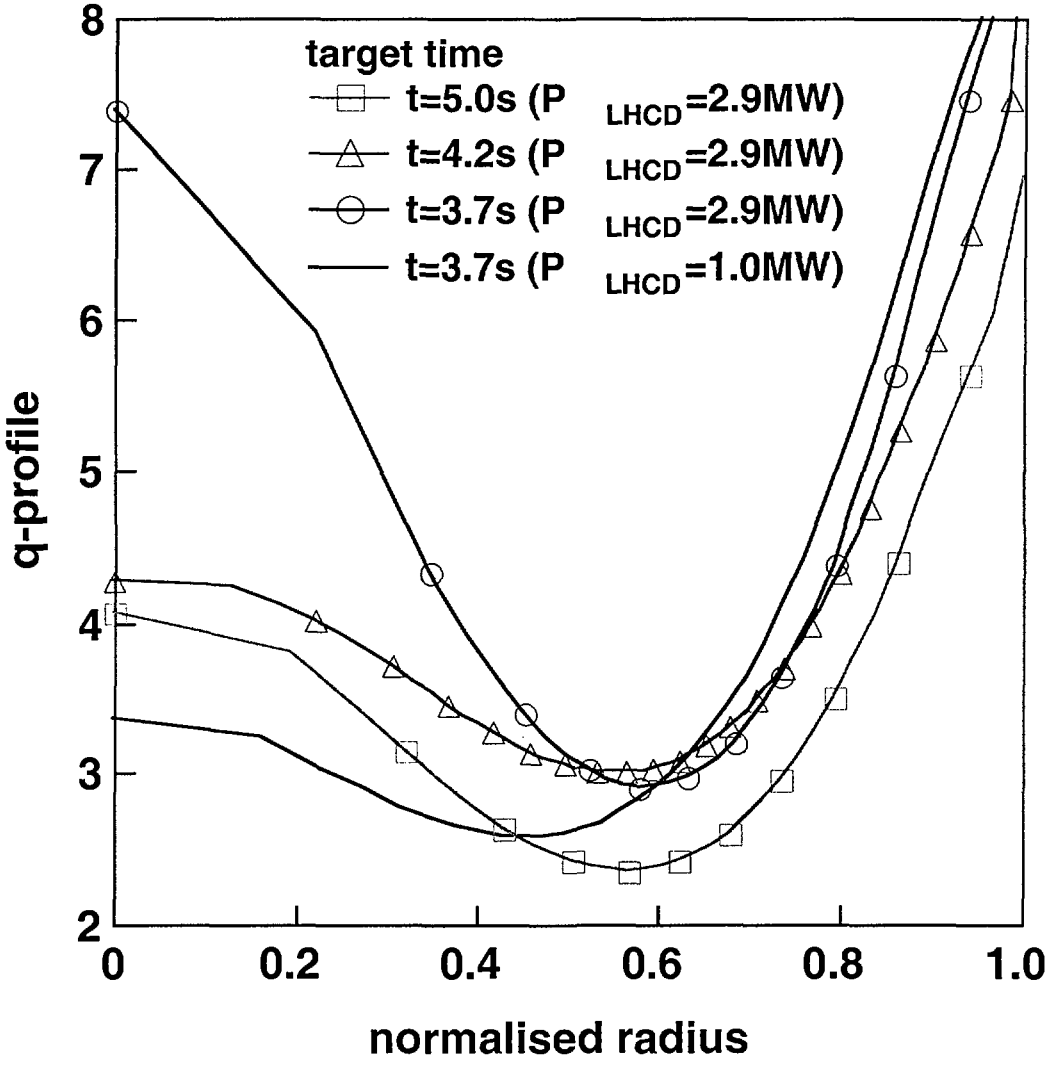
target time
t=5.0s (P LHCD=2.9MW)
t=4.2s (P LHCD=2.9MW)
t=3.7s (P LHCD=2.9MW)
t=3.7s (P LHCD=1.0MW)
q-profile
normalised radius
8
7
6
5
4
3
2
0
0.2
0.4
0.6
0.8
1.0

Figure 8

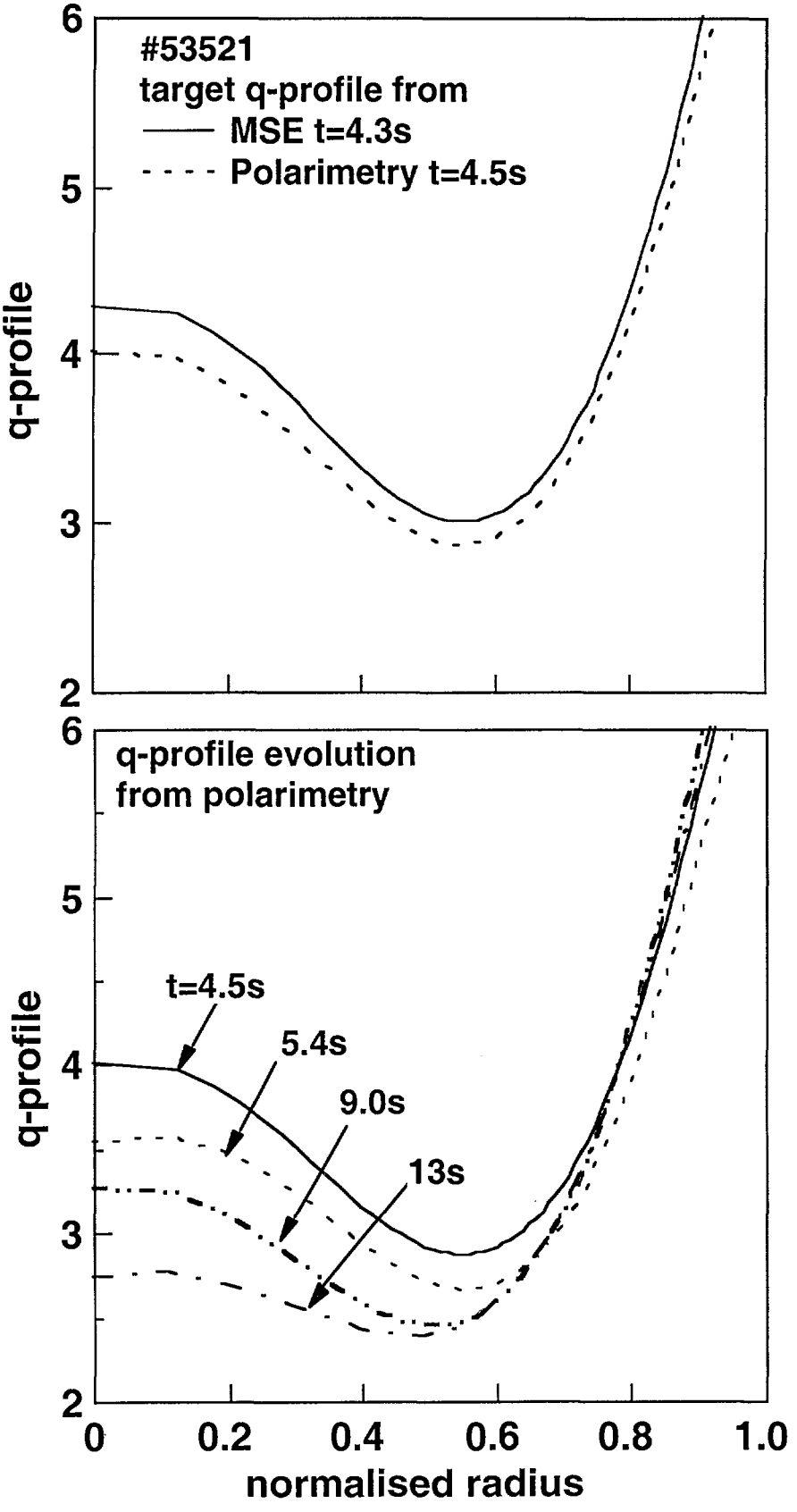
#53521
target q-profile from
MSE t=4.3s
Polarimetry t=4.5s
q-profile
6
5
4
3
2
q-profile evolution
from polarimetry
t=4.5s
5.4s
9.0s
13s
0
0.2
0.4
0.6
0.8
1.0
normalised radius

Figure 9

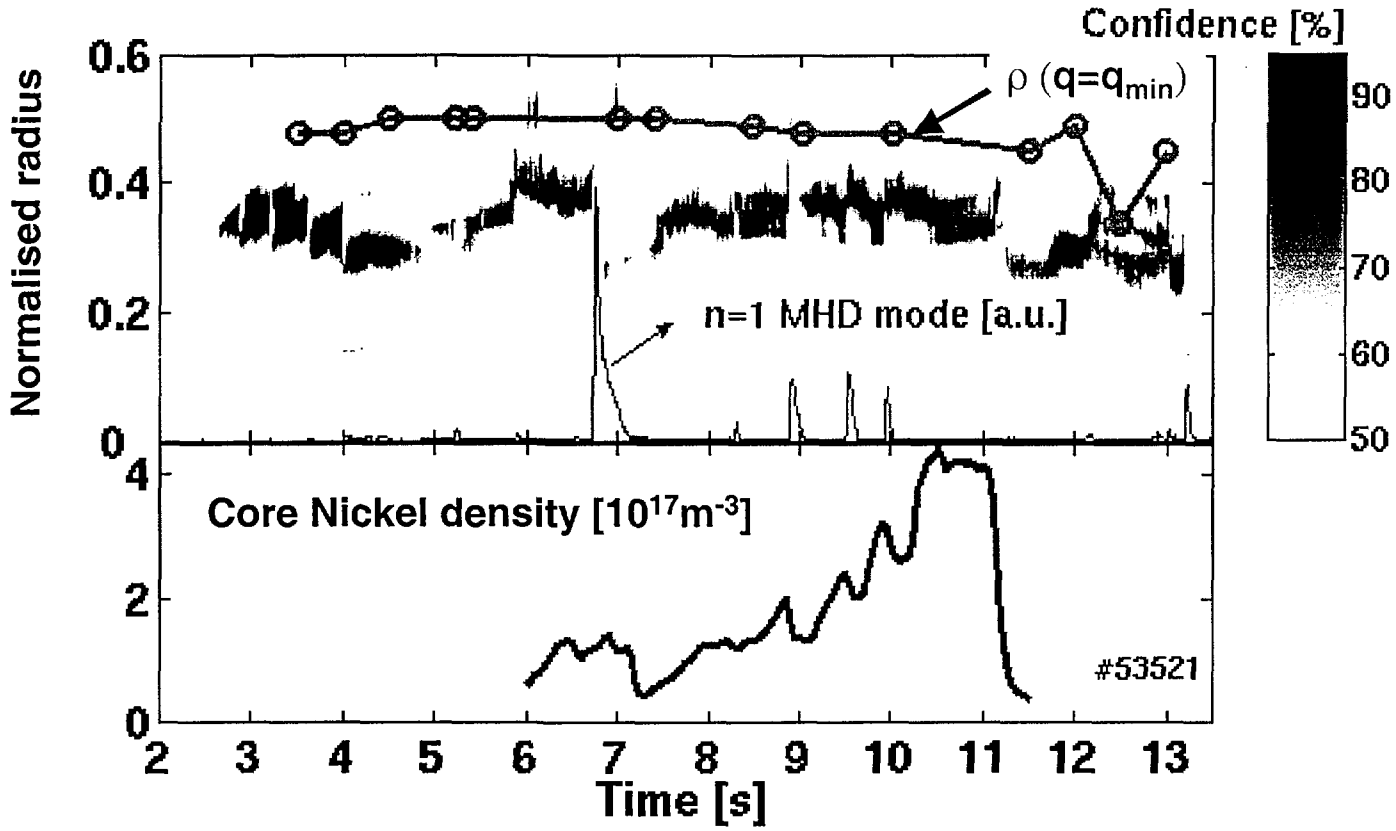
Confidence [%]
Normalised radius
0.6
0.4
0.2
0
ρ (q=q_min)
n=1 MHD mode [a.u.]
90
80
70
60
50
4
2
0
Core Nickel density [10^17m^-3]
#53521
2 3 4 5 6 7 8 9 10 11 12 13
Time [s]

Figure 10

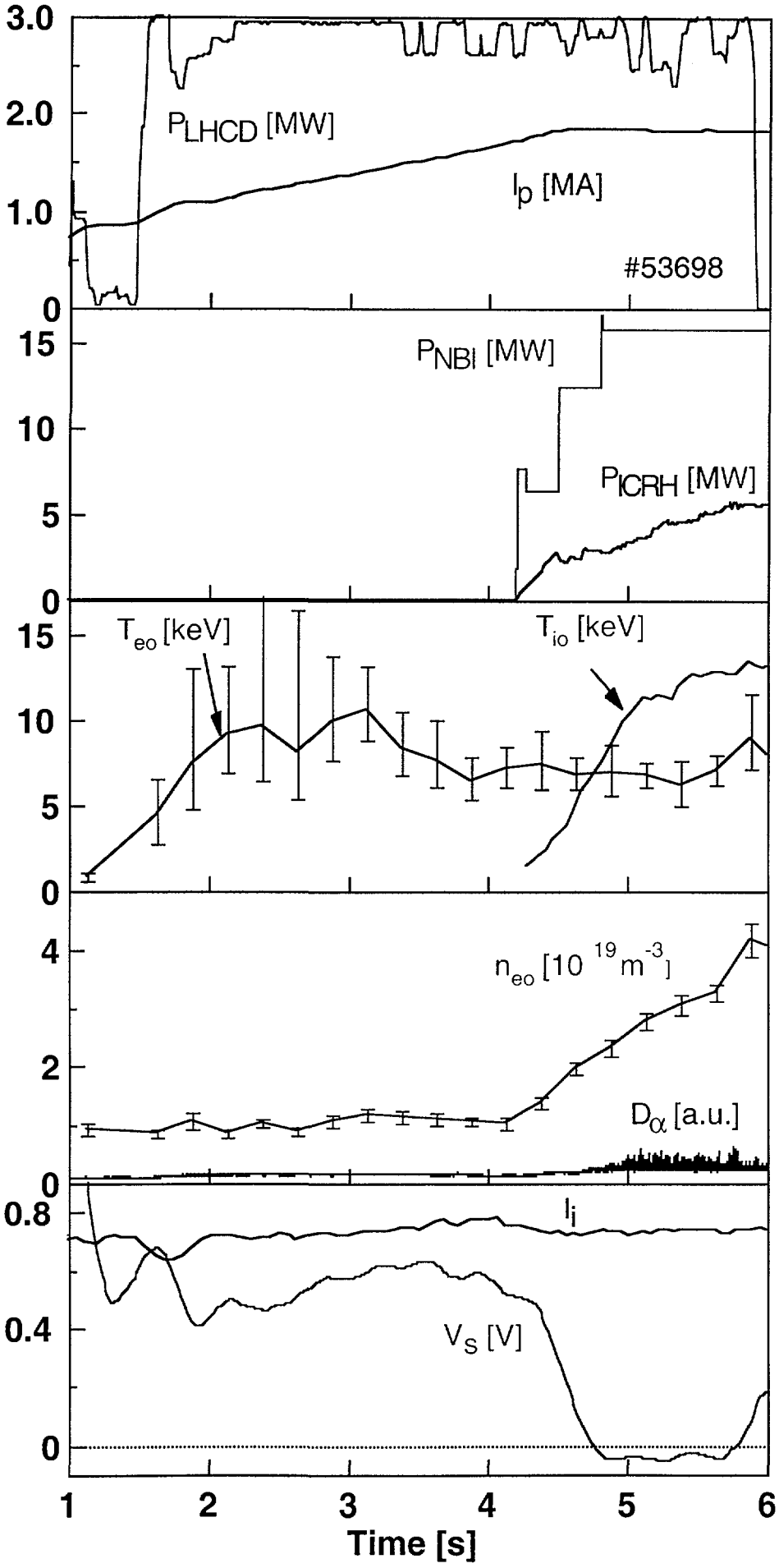
3.0
2.0
1.0
0
P_{LHCD} [MW]
I_p [MA]
#53698
15
10
5
0
P_{NBI} [MW]
P_{ICRH} [MW]
15
10
5
0
T_{eo} [keV]
T_{io} [keV]
4
2
0
n_{eo} [10^{19} m^{-3}]
D_α [a.u.]
0.8
0.4
0
l_i
V_S [V]
1
2
3
4
5
6
Time [s]

Figure 11

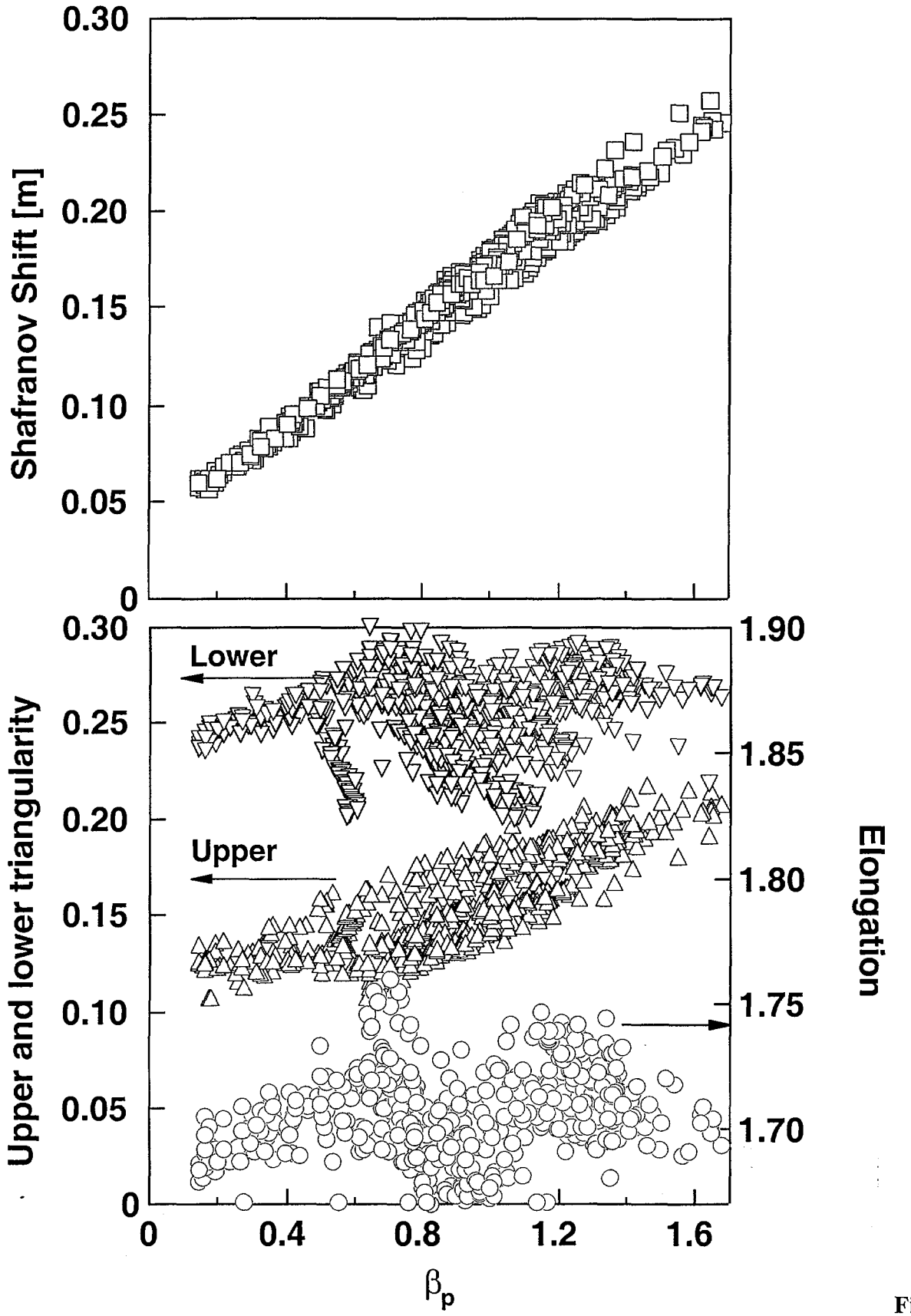
Shafranov Shift [m]
0.30
0.25
0.20
0.15
0.10
0.05
0
Upper and lower triangularity
Lower
Upper
1.90
1.85
1.80
1.75
1.70
Elongation
0
0.4
0.8
1.2
1.6
β_p

Figure 12

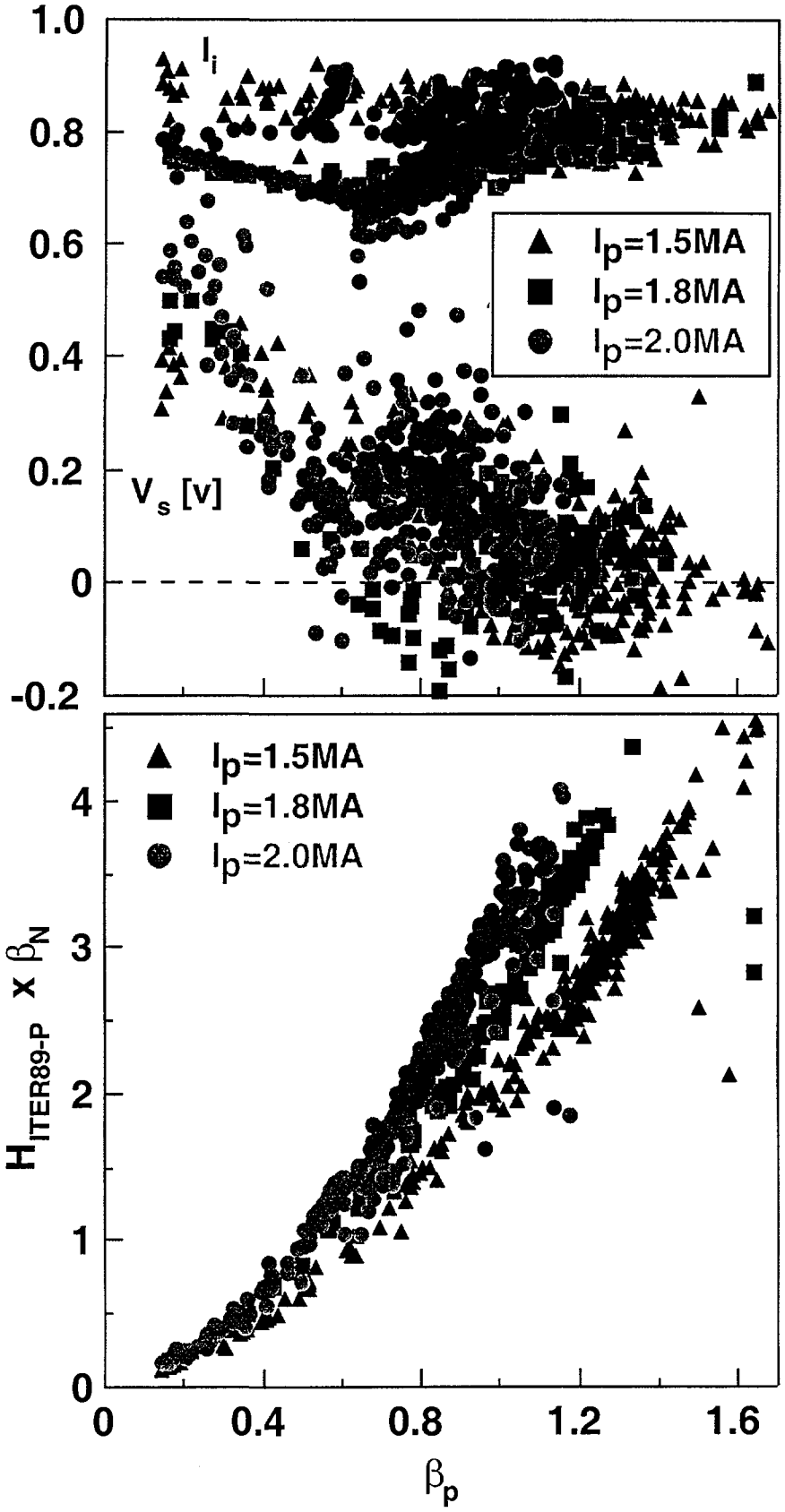
1.0
0.8
0.6
0.4
0.2
0
-0.2
l_i
I_p=1.5MA
I_p=1.8MA
I_p=2.0MA
V_s [v]
4
3
2
1
0
$H_{ITER89-P}$ x β_N
0
0.4
0.8
1.2
1.6
β_p

Fig. 13

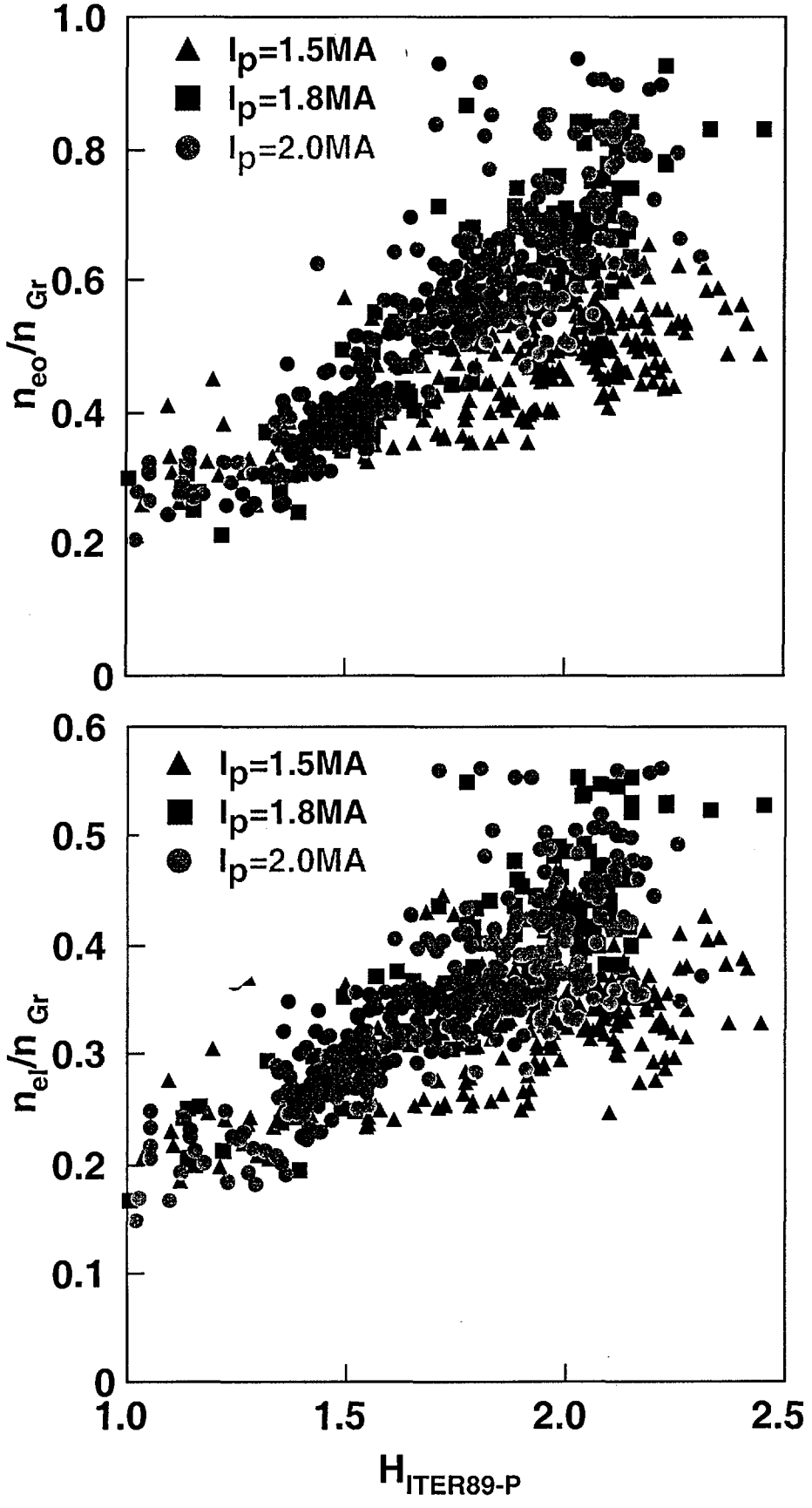
1.0
0.8
0.6
0.4
0.2
0
n_{eo}/n_{Gr}
I_p=1.5MA
I_p=1.8MA
I_p=2.0MA
0.6
0.5
0.4
0.3
0.2
0.1
0
n_{el}/n_{Gr}
I_p=1.5MA
I_p=1.8MA
I_p=2.0MA
1.0
1.5
2.0
2.5
$H_{ITER89-P}$

Figure 14-a

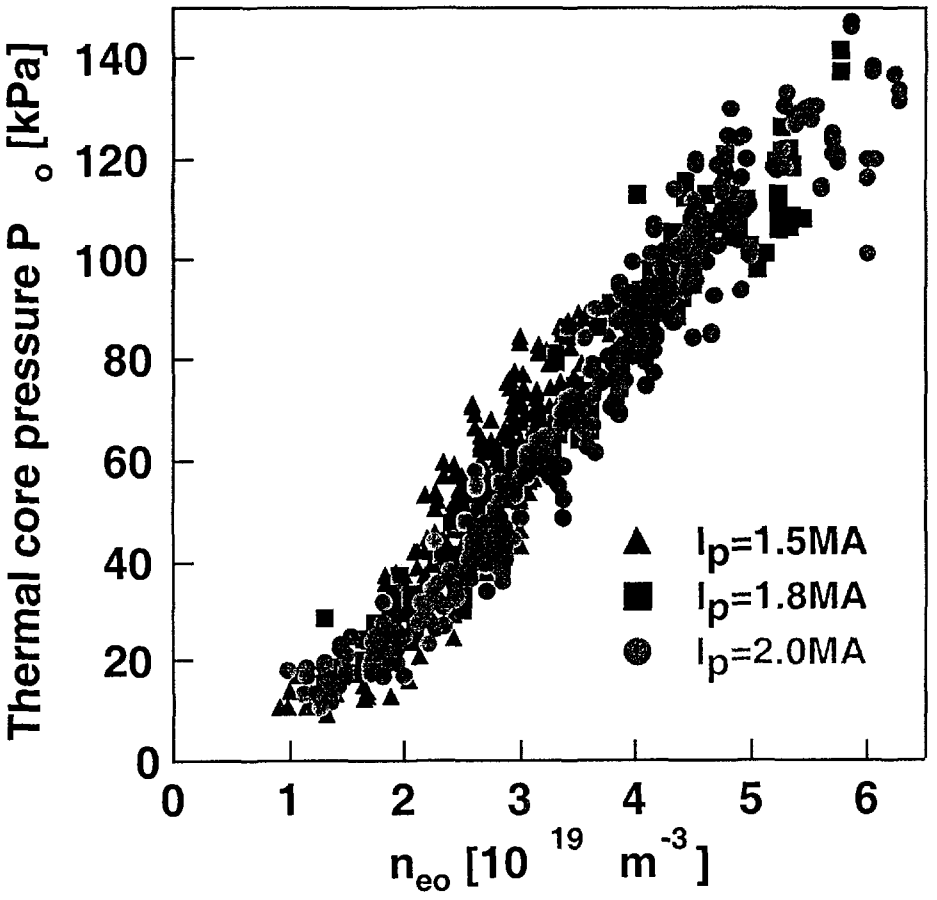
Thermal core pressure P o [kPa]
140
120
100
80
60
40
20
0
0
1
2
3
4
5
6
n_eo [10 19 m -3]
I_p=1.5MA
I_p=1.8MA
I_p=2.0MA

Figure 14-b

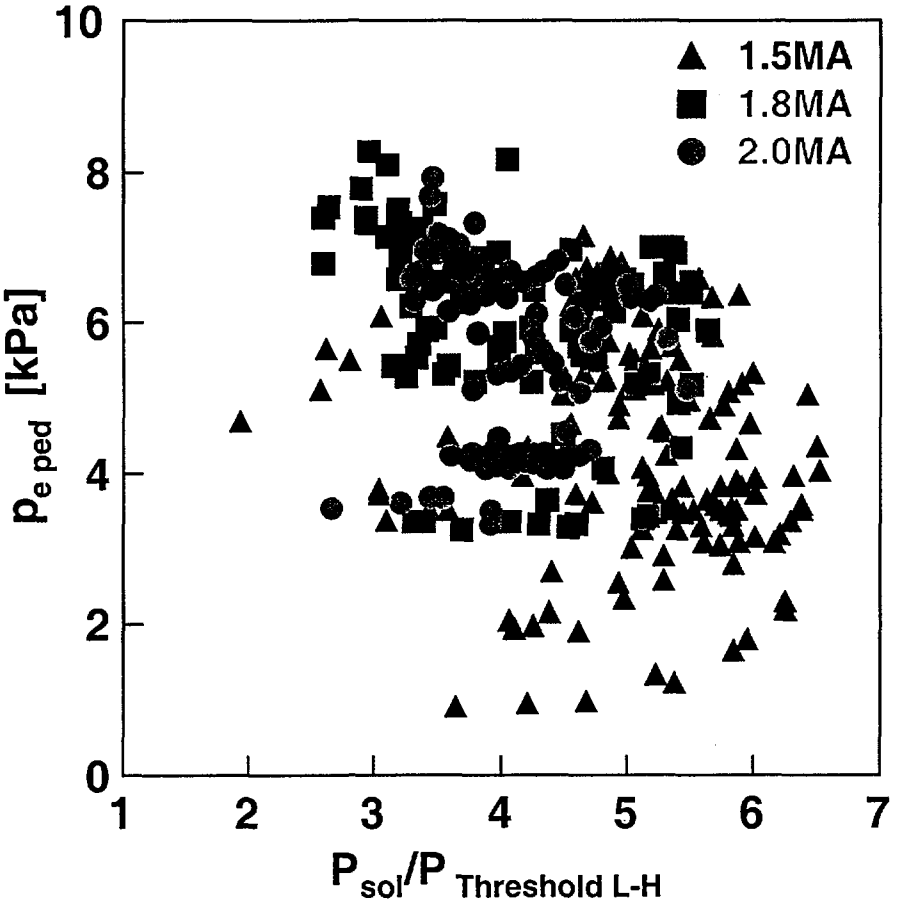
1.5MA
1.8MA
2.0MA
$p_{e\ ped}$ [kPa]
$P_{sol}/P_{Threshold\ L-H}$
0
2
4
6
8
10
1
2
3
4
5
6
7

Figure 15

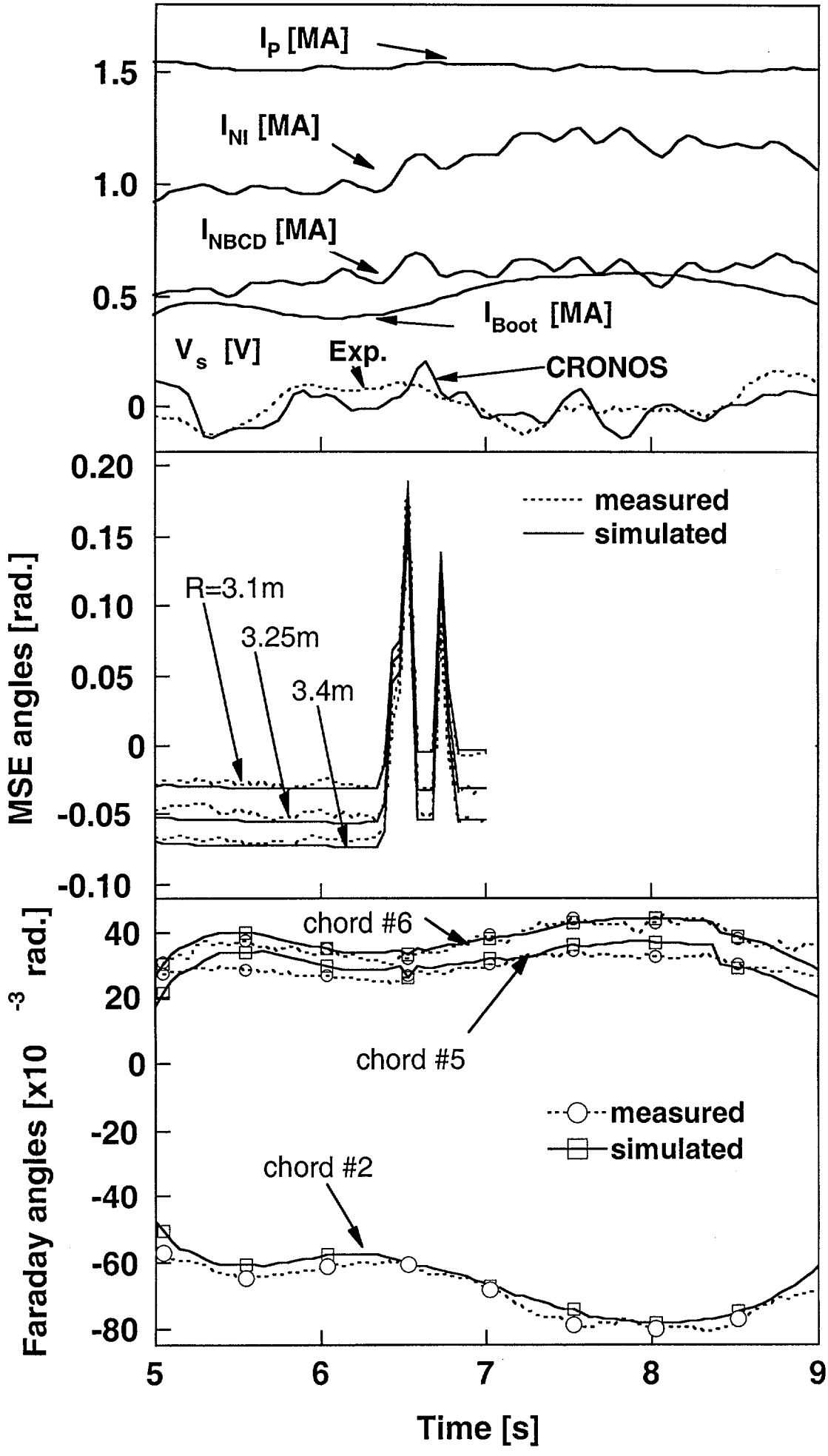
I_P [MA]
I_{NI} [MA]
I_{NBCD} [MA]
I_{Boot} [MA]
V_s [V]
Exp.
CRONOS
1.5
1.0
0.5
0
measured
simulated
R=3.1m
3.25m
3.4m
MSE angles [rad.]
0.20
0.15
0.10
0.05
0
-0.05
-0.10
chord #6
chord #5
chord #2
measured
simulated
Faraday angles [x10^{-3} rad.]
40
20
0
-20
-40
-60
-80
5
6
7
8
9
Time [s]

Figure 16-a

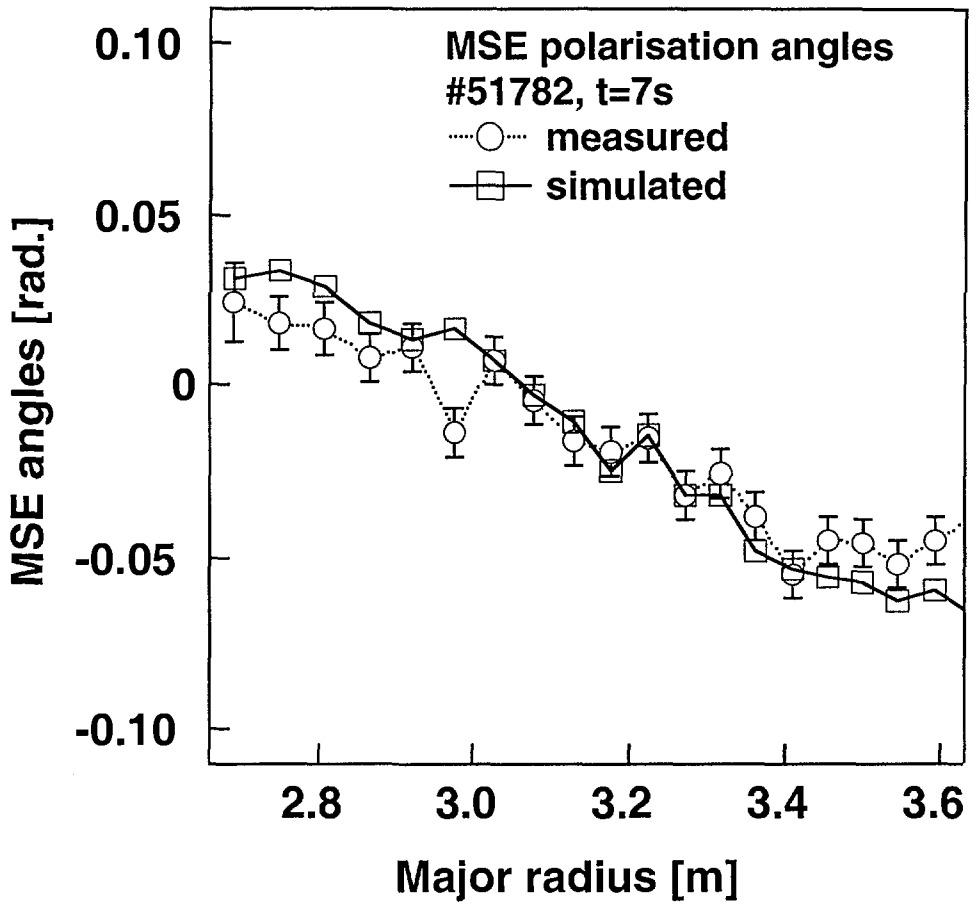
MSE polarisation angles
#51782, t=7s
measured
simulated
0.10
0.05
0
-0.05
-0.10
MSE angles [rad.]
2.8
3.0
3.2
3.4
3.6
Major radius [m]

Figure 16-b

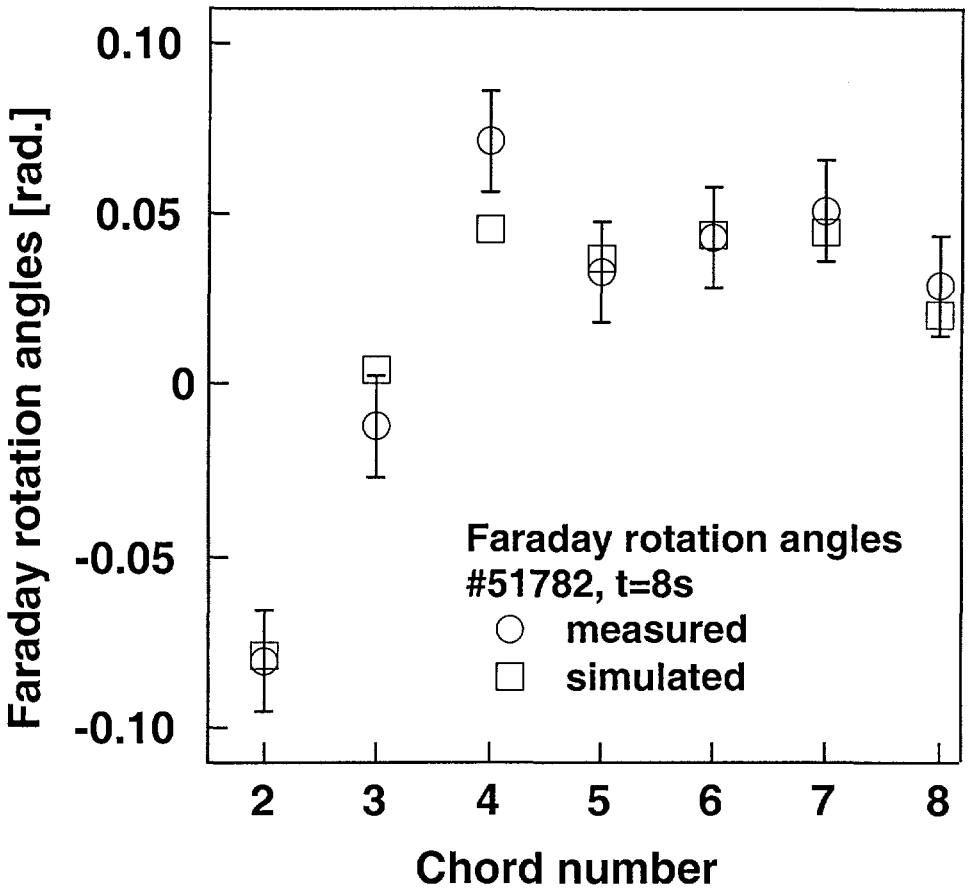
0.10
0.05
0
-0.05
-0.10
Faraday rotation angles [rad.]
2
3
4
5
6
7
8
Chord number
Faraday rotation angles
#51782, t=8s
measured
simulated

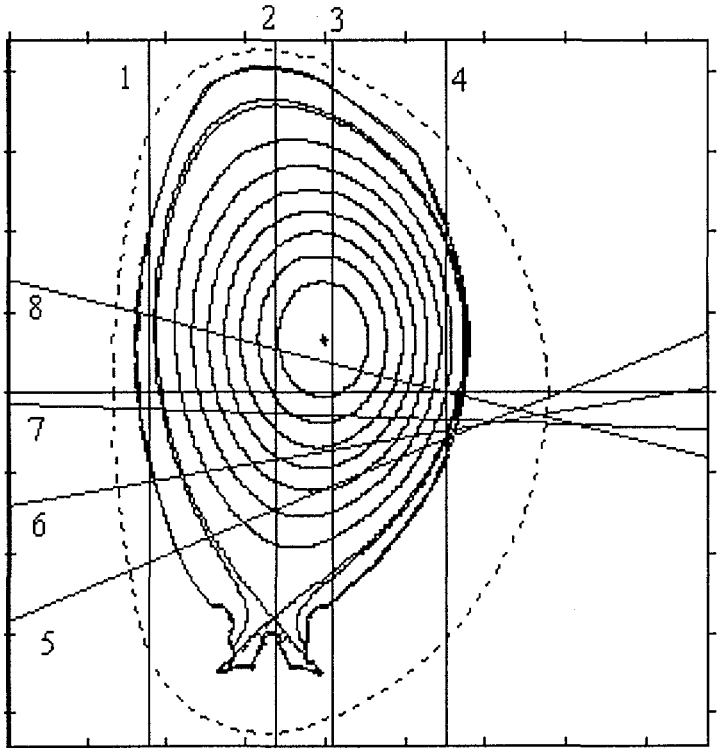
1
2
3
4
5
6
7
8

Figure 16-c

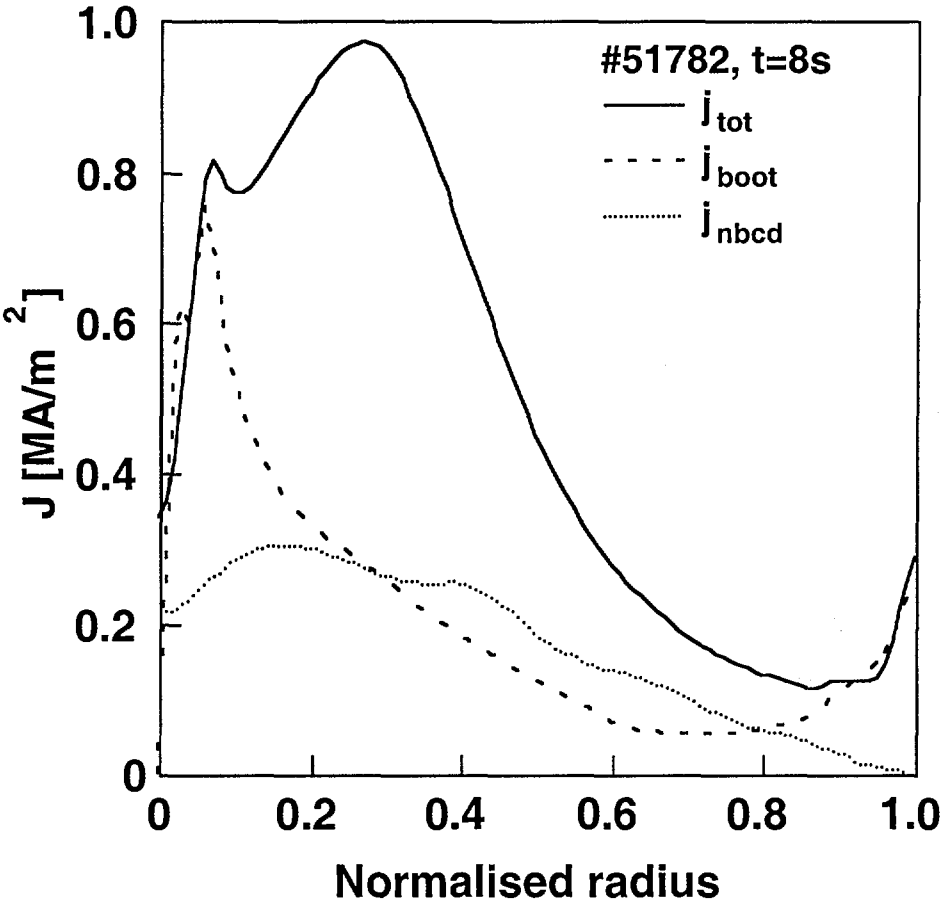
#51782, t=8s
j tot
j boot
j nbcd
J [MA/m 2]
Normalised radius
0
0.2
0.4
0.6
0.8
1.0

Figure 17

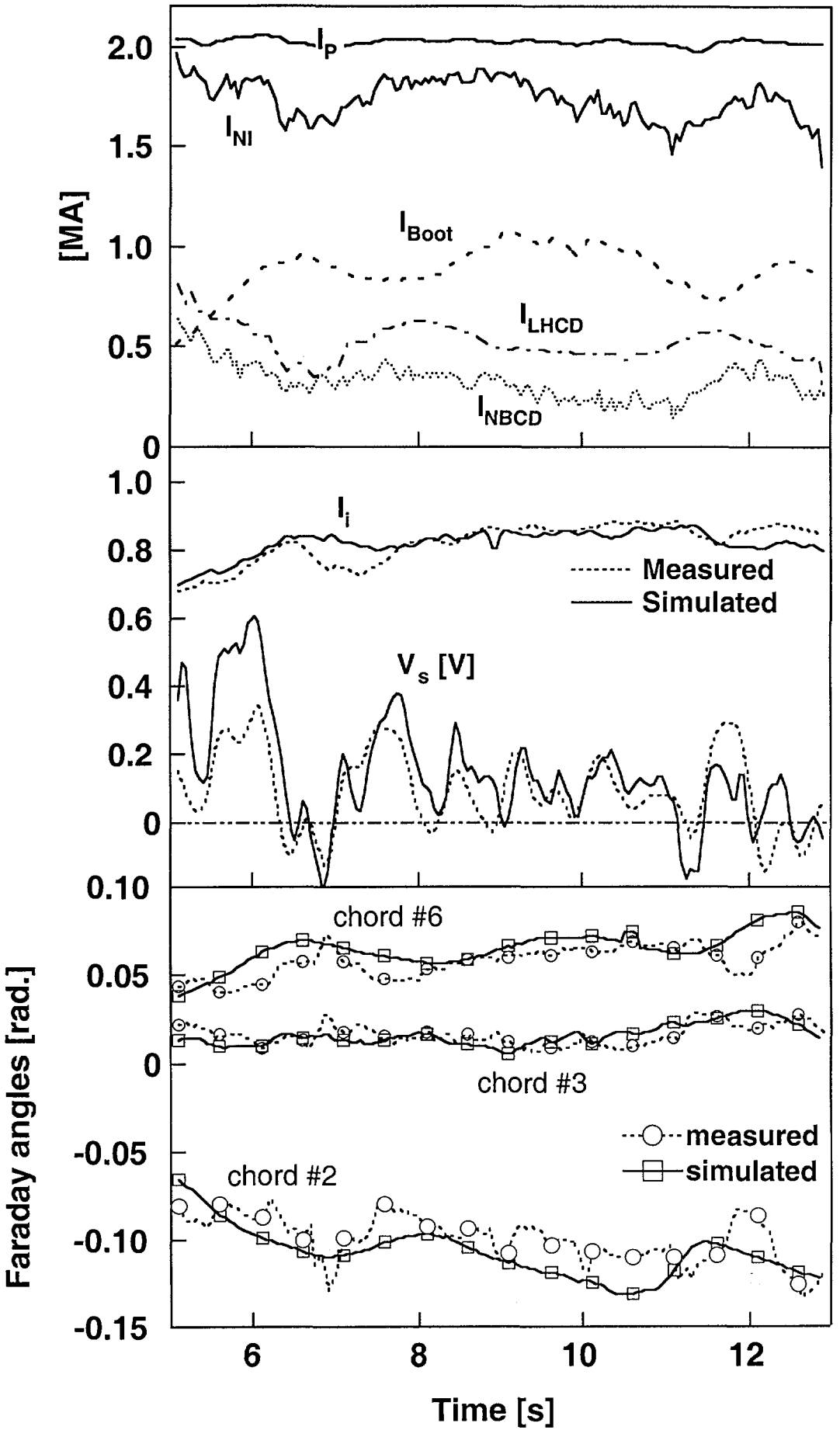
2.0
1.5
1.0
0.5
0
[MA]
I_P
I_{NI}
I_{Boot}
I_{LHCD}
I_{NBCD}
1.0
0.8
0.6
0.4
0.2
0
I_i
Measured
Simulated
V_s [V]
0.10
0.05
0
-0.05
-0.10
-0.15
Faraday angles [rad.]
chord #6
chord #3
chord #2
measured
simulated
6
8
10
12
Time [s]

Figure 18-a

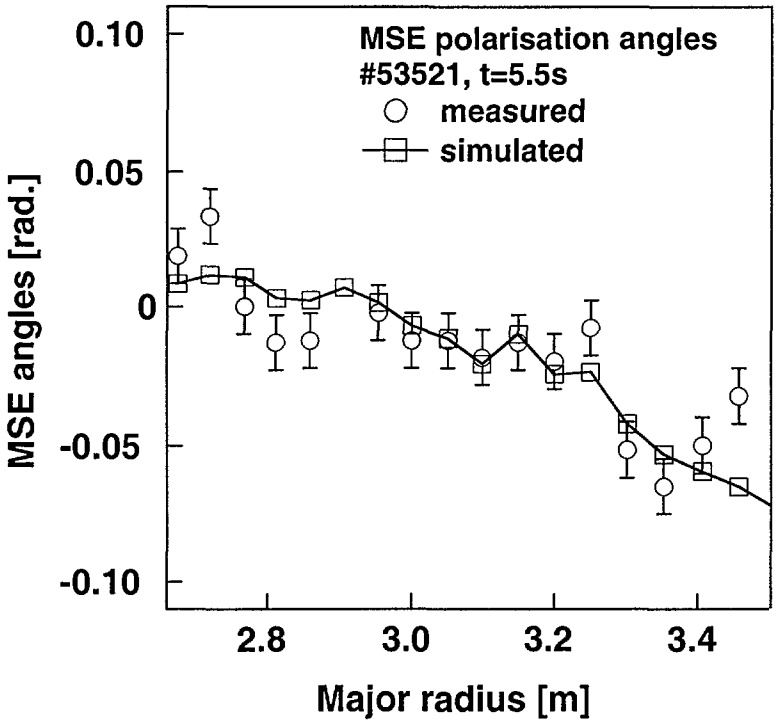

Figure 18-b

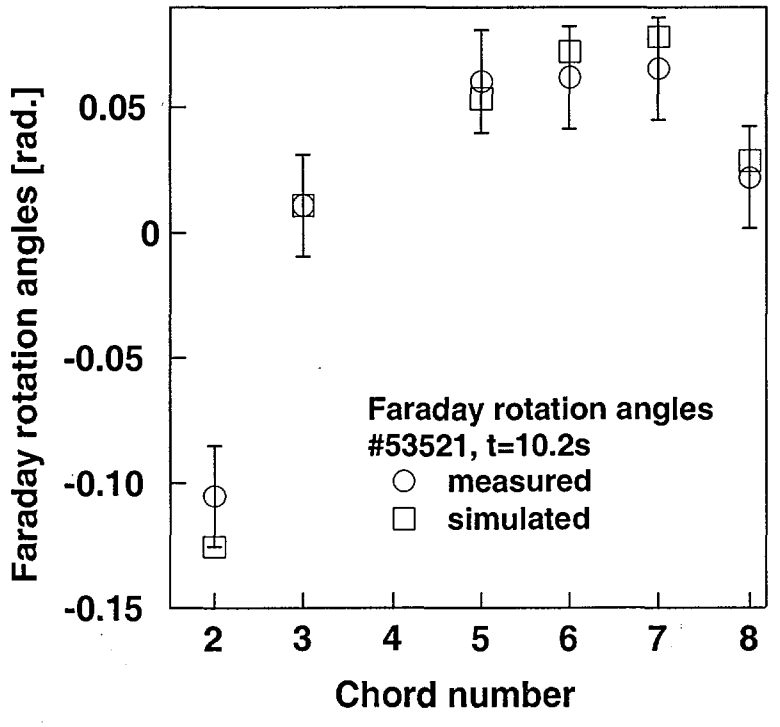

Figure 18-c

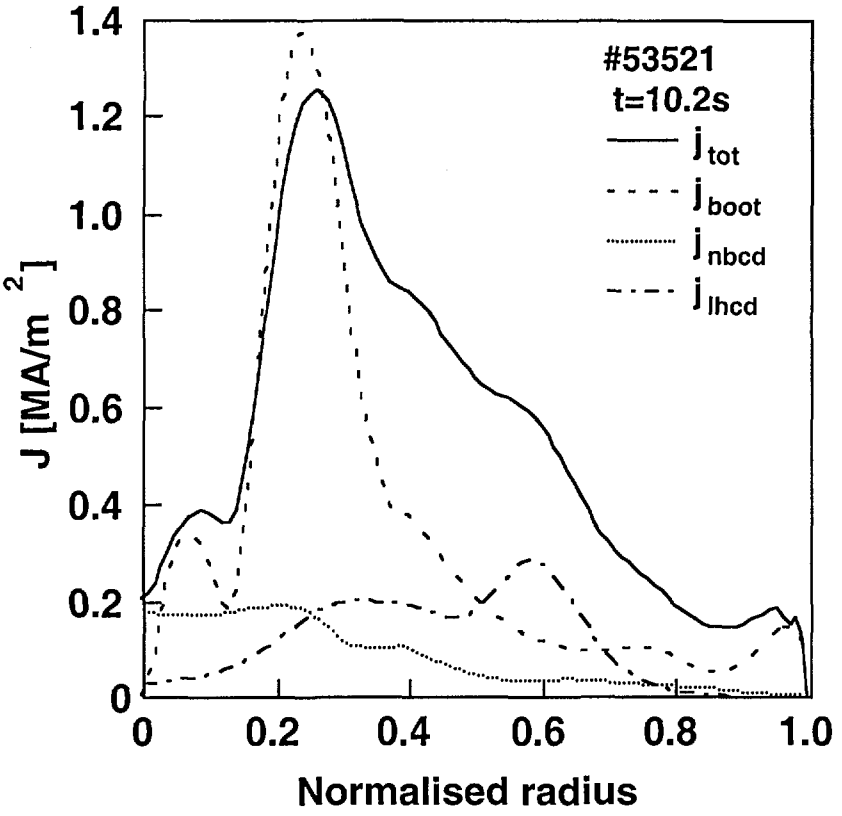
#53521
t=10.2s
j tot
j boot
j nbcd
j lhcd
J [MA/m 2]
Normalised radius
0
0.2
0.4
0.6
0.8
1.0
1.2
1.4

Figure 19

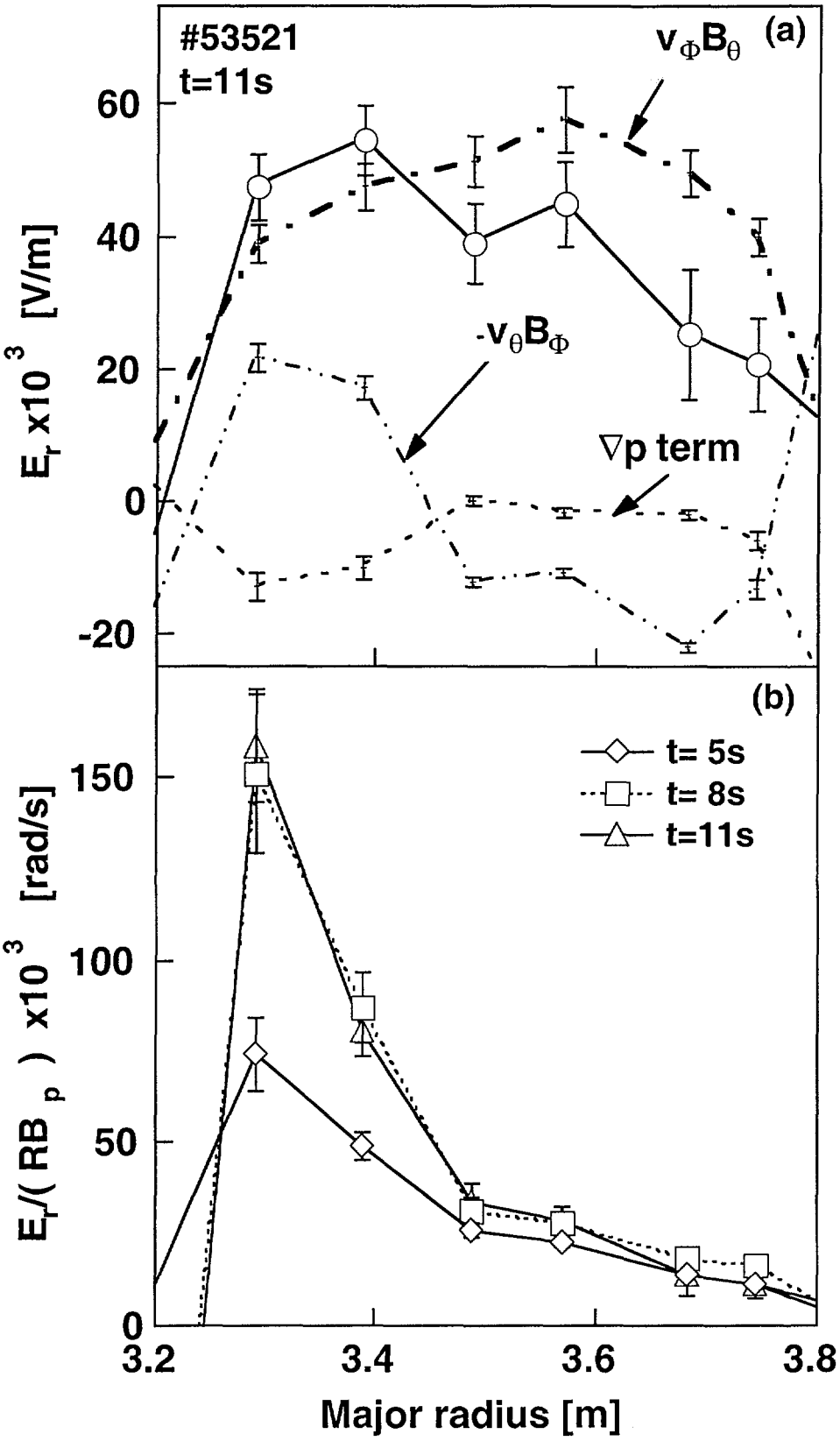
#53521
t=11s
$v_\Phi B_\theta$ (a)
$-v_\theta B_\Phi$
∇p term
E_r x10^3 [V/m]
60
40
20
0
-20
(b)
t= 5s
t= 8s
t=11s
$E_r/(RB_p)$ x10^3 [rad/s]
150
100
50
0
3.2
3.4
3.6
3.8
Major radius [m]

Figure 20

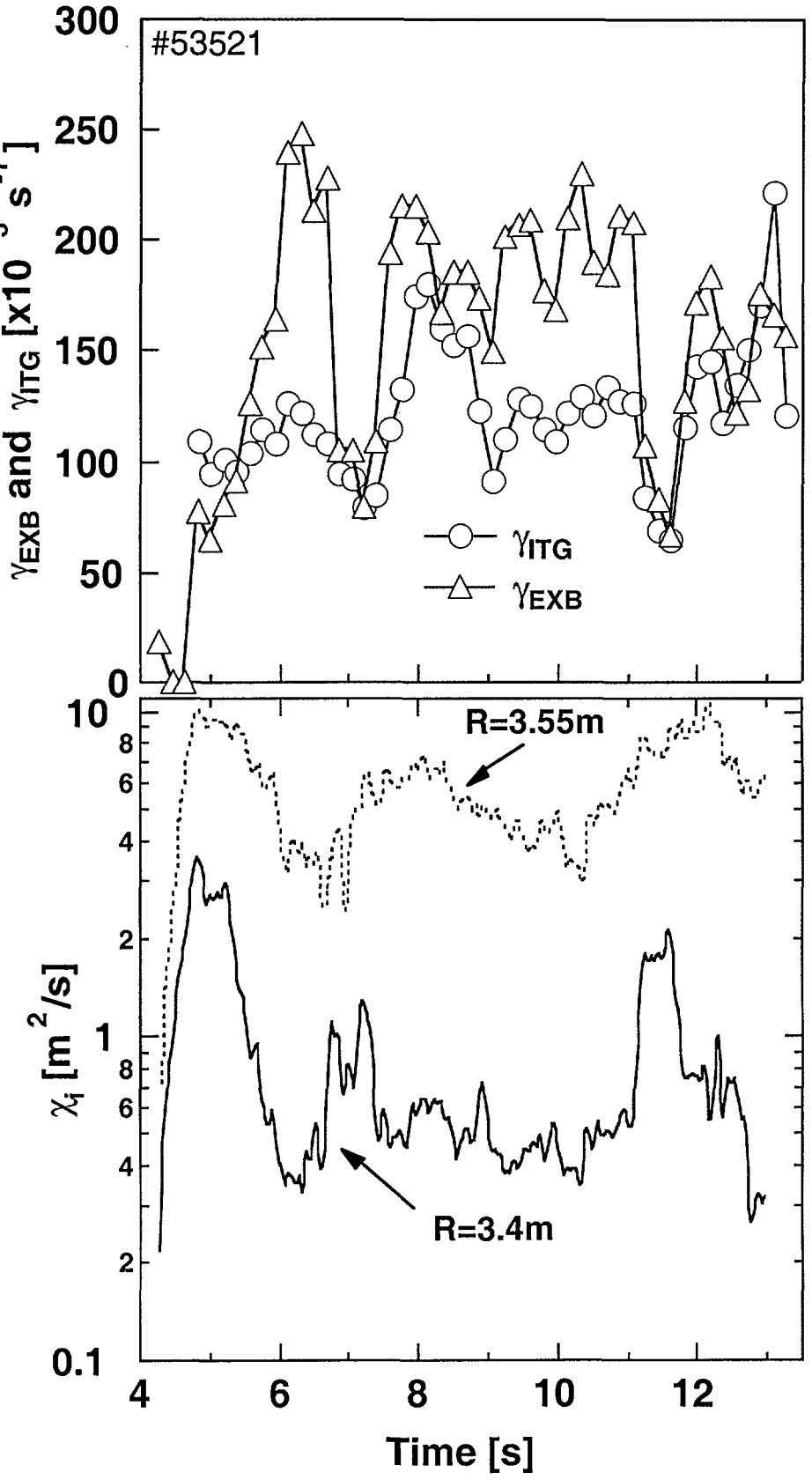
#53521
γ_{EXB} and γ_{ITG} [x10^3 s^{-1}]
γ_{ITG}
γ_{EXB}
R=3.55m
R=3.4m
χ_i [m^2/s]
Time [s]

Figure 21

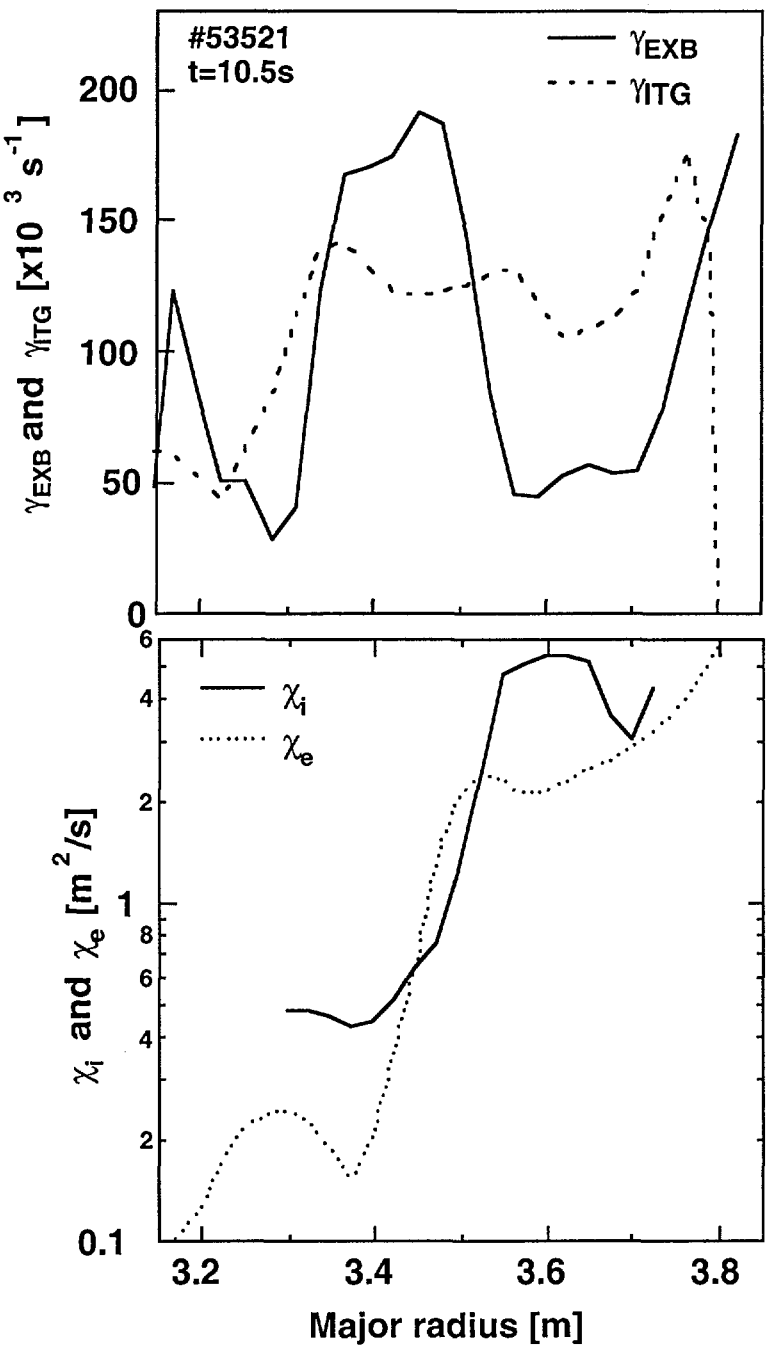
#53521
t=10.5s
γEXB
γITG
γEXB and γITG [x10 3 s-1]
200
150
100
50
0
χi
χe
χi and χe [m2/s]
6
4
2
1
8
6
4
2
0.1
3.2
3.4
3.6
3.8
Major radius [m]

Figure 22

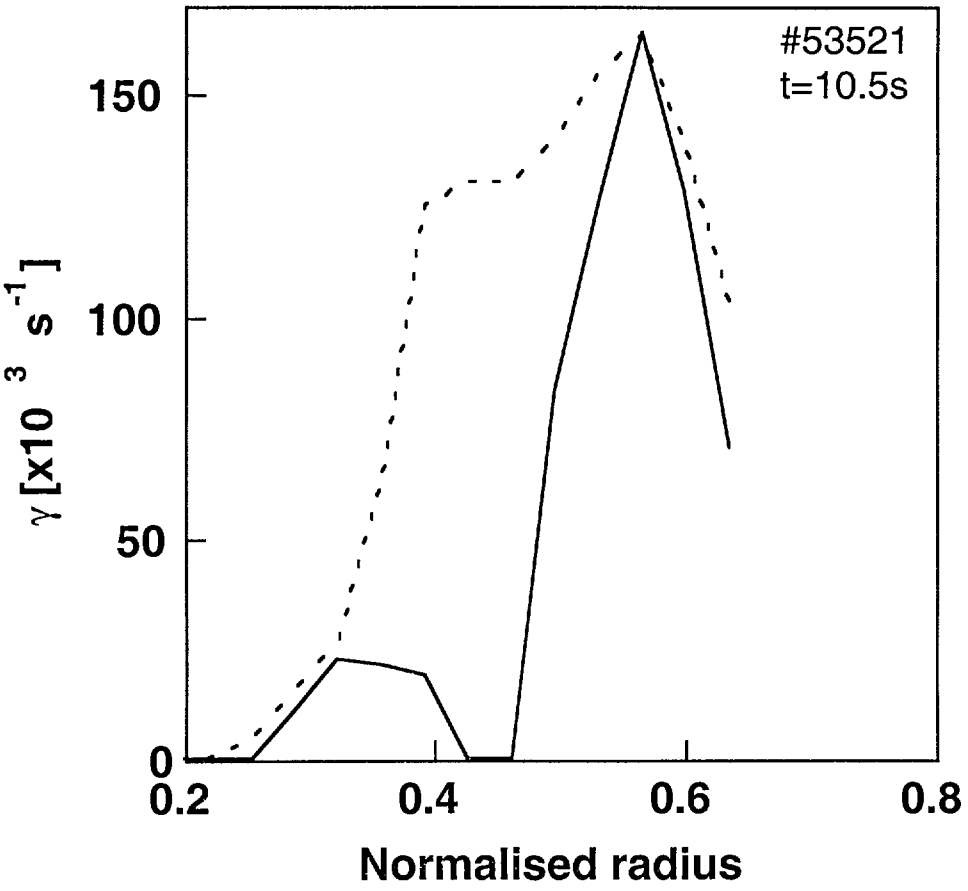
#53521
t=10.5s
150
100
50
0
0.2
0.4
0.6
0.8
γ [x10 3 s -1]
Normalised radius

Figure 23